

Multi-Scenario Broadband Channel Measurement and Modeling for Sub-6 GHz RIS-Assisted Wireless Communication Systems

Jian Sang¹, Graduate Student Member, IEEE, Mingyong Zhou, Jifeng Lan, Graduate Student Member, IEEE, Boning Gao, Wankai Tang², Member, IEEE, Xiao Li³, Member, IEEE, Shi Jin⁴, Senior Member, IEEE, Ertugrul Basar⁵, Fellow, IEEE, Cen Li, Qiang Cheng⁶, Senior Member, IEEE, and Tie Jun Cui⁷, Fellow, IEEE

Abstract—Reconfigurable intelligent surface (RIS)-empowered communication, has been considered widely as one of the revolutionary technologies for next generation networks. However, due to the novel propagation characteristics of RISs, underlying RIS channel modeling and measurement research is still in its infancy and not fully investigated. In this paper, we conduct multi-scenario broadband channel measurements and modeling for RIS-assisted communications at the sub-6 GHz band. The measurements are carried out in three scenarios covering outdoor, indoor, and outdoor-to-indoor (O2I) environments, which suffer from non-line-of-sight (NLOS) propagation inherently. Three propagation modes including intelligent reflection with RIS, specular reflection with RIS and the mode without RIS, are taken into account in each scenario. In addition, considering the cascaded characteristics of RIS-assisted channel by nature, two modified empirical models including floating-intercept (FI) and close-in (CI) are proposed, which cover distance and angle domains. The measurement results rooted in 2096 channel acquisitions verify the prediction accuracy of these proposed models. Moreover, the propagation characteristics for RIS-assisted channels, including path loss (PL) gain, PL exponent, spatial consistency,

time dispersion, frequency stationarity, etc., are compared and analyzed comprehensively. These channel measurement and modeling results may lay the groundwork for future applications of RIS-assisted communication systems in practice.

Index Terms—RIS-assisted systems, channel measurement, channel modeling, sub-6 GHz.

I. INTRODUCTION

WITH the deployment of the fifth generation (5G) communication networks around the world since 2019, the global mobile data traffic has experienced a dramatic growth, which is anticipated to reach 5016 exabytes per month (Eb/mo) in 2030 [1]. The evolutionary and advanced sixth generation (6G) communication networks with the even higher requirements, have aroused a surge of interest from both academia and industry nowadays. By 6G networks, many emerging application services such as virtual reality, holographic telepresence, pervasive connectivity, etc., are envisioned to be realized [2], [3]. Up to now, although no detailed specifications have been laid out on the communication standard of 6G, the study of possible innovating technologies, applicable propagation model and practical channel measurement facing 6G, have been the focus of initiatives in various countries [4], [5].

Reconfigurable intelligent surface (RIS)-empowered communication, with its ability of controlling the propagation environment effectively, has recently been considered one of the revolutionary technologies to meet the ever-increasing 6G demands [6], [7]. RIS provides a prospective concept by manipulating the electromagnetic (EM) wave which is impinging on it and reflected to the desired direction, with a relatively low power consumption. By this means, RIS can constructively customize wireless channels instead of traditionally adapting to the harsh propagation environment [8].

Generally speaking, an RIS is composed of an artificial meta-surface with plentiful sub-wavelength sized unit cells arranged in an array form. The reflection coefficients of each unit cell, e.g., magnitude, phase, polarization, etc., can be reconfigured intelligently through adjusting the control voltage [9]. Typically, each unit cell is comprised of conductive printed patch, which has a size of proportion to the wavelength of operating frequency. In order to reconfigure

Manuscript received 28 March 2023; revised 27 July 2023 and 2 October 2023; accepted 27 October 2023. Date of publication 15 November 2023; date of current version 12 June 2024. This work was supported in part by the National Natural Science Foundation of China under Grant 62231009, Grant 61971126, Grant 62261160576, Grant 62288101, and Grant 62201138; in part by the Natural Science Foundation of Jiangsu Province under Grant BK20211511 and Grant BK20220809; in part by the Jiangsu Province Frontier Leading Technology Basic Research Project under Grant BK20212002; in part by the Start-Up Research Fund of Southeast University under Grant RF1028623267; and in part by the Scientific and Technological Research Council of Turkey (TUBITAK) under Grant 120E401. The associate editor coordinating the review of this article and approving it for publication was A. G. Kanatas. (Corresponding author: Xiao Li.)

Jian Sang, Mingyong Zhou, Jifeng Lan, Boning Gao, Wankai Tang, Xiao Li, and Shi Jin are with the National Mobile Communications Research Laboratory, Southeast University, Nanjing 210012, China (e-mail: sangjian@seu.edu.cn; myzhou@seu.edu.cn; lanjifeng@seu.edu.cn; gaobn@seu.edu.cn; tangwk@seu.edu.cn; li_xiao@seu.edu.cn; jinshi@seu.edu.cn).

Ertugrul Basar is with the Communications Research and Innovation Laboratory (CoreLab), Department of Electrical and Electronics Engineering, Koç University, Sariyer, 34450 Istanbul, Turkey (e-mail: ebasar@ku.edu.tr).

Cen Li is with China Information Consulting Designing Institute Company Ltd., Nanjing 210012, China (e-mail: licen.jszyj@chinaccs.cn).

Qiang Cheng and Tie Jun Cui are with the State Key Laboratory of Millimeter Waves, Southeast University, Nanjing 210012, China (e-mail: qiangcheng@seu.edu.cn; tjcui@seu.edu.cn).

Color versions of one or more figures in this article are available at <https://doi.org/10.1109/TWC.2023.3330977>.

Digital Object Identifier 10.1109/TWC.2023.3330977

the EM response, a tunable load, such as positive-intrinsic-negative (PIN) diode or varactor diode, could be embedded into unit cell to interact with control voltage. In this way, the EM characteristics of the outgoing signal can be programmed independently by a smart controller such as field programmable gate array (FPGA) in real time. Thanks to such innovative characteristics brought by RISs, the radio propagation environment may be redefined [10], [11].

Until now, numerous analyses on RIS-empowered systems have been theoretically investigated in many fields, including but not limited to: user localization [12], secure communication [13], beam optimization [14], user scheduling [15], etc. Meanwhile, free-space channel modeling as well as power-related measurements for RIS-assisted non-line-of-sight (NLOS) communications have gradually been reported [16], [17]. Nevertheless, the real channel measurement campaign and applicable channel model in practice, which describe the underlying physical propagation phenomena of EM waves incurred by RIS, are still in their infancy and rarely proposed, despite their critical roles.

A. Modeling-Related Works

Considering broadcast and beamforming scenarios respectively, [18] and [19] theoretically formulated the path loss (PL) expressions for RIS-assisted NLOS communications in free space. Then a two-path propagation model for RIS-assisted communications was proposed in [20], which showed that the deployment of RIS was advantageous for mitigating fast fading. In [21], a physics-driven PL model for RIS-assisted link in free space was proposed based on antenna theory. In [22], the PL scaling law of the scattered field was discussed numerically, which unified the opposite behavior of RIS serving as a scatterer and a mirror. Reference [23] formulated the RIS-related PL models by using the vector generalization of Green's theorem. In [24], a PL model for RIS-assisted systems was proposed based on physical optics technique, which explained the mechanism why the plentiful unit cells on RIS individually acted as diffuse scatterers but could jointly perform beamforming in a desired direction. Reference [25] considered that RIS were partitioned into several tiles, which yielded the free-space tile response model for RIS-assisted link. In [26], an RIS channel simulator was introduced by considering the 3GPP channel modeling methodology for millimeter wave (mmWave) channels.

In addition to the PL model, a few geometry-based stochastic models (GBSMs) have also been developed for RIS-related channel modeling. In [27] and [28], a near-field RIS-assisted multiple-input multiple-output (MIMO) channel model was proposed based on a three-dimensional (3D) cylinder model, which considered line-of-sight (LOS), single-bounced and double-bounced modes. In [29], a 3D GBSM for a massive MIMO communication system employing practical discrete RIS was proposed, which enabled the mobility of the transceivers as well as environments. A wideband non-stationary channel model for RIS-assisted MIMO communication was developed in [30]. This model investigated the sub-channel characteristics between the transmitter (Tx), RIS, and receiver (Rx).

B. Measurement-Related Works

In [18], Tang et al. conducted the measurements to validate PL models in an anechoic chamber, utilizing three RISs at 4.25 GHz and 10.5 GHz respectively. Further mmWave measurements on two customized RIS covering 27 GHz and 33 GHz were carried out in [19] to verify the refined PL models. In [31], two RISs constituted of varactor diodes and PIN diodes respectively, were employed in an indoor environment to illustrate the RIS-related channel reciprocity. By utilizing universal software radio peripherals (USRPs), the measurement campaigns in [32] illustrated that an RIS could bring a power gain of 27 dB and 14 dB for short-range and long-range communications, respectively. In [33], a signal-to-noise ratio (SNR) gain of 8 dB was shown to be offered by the RIS at 5.8 GHz when the NLOS distance reached 35 m. Reference [34] proposed a spectrum sharing solution using RIS in indoor channel, where experiments conducted at 2.4 GHz demonstrated a higher spectrum-spatial efficiency by controlling the phase shifts of RIS. A 1-bit RIS fabricated in [35] validated its capability of enhancing power gains by conducting the indoor measurements at 3.5 GHz. In [36], the experiments conducted on a multi-bit RIS substantiated a power improvement of 2.65 dB compared with 1-bit RIS. In [37], the RIS experiments at 28 GHz manifested its capability for transmission signal enhancement in NLOS links. Considering the RIS serving as Tx, the measurements at 28 GHz in [38] illustrated that the PL in the main beam directions were improved by RIS. Reference [39] considered practical measurements at 5 GHz and employed RIS codebooks to dynamically adjust the RIS phases depending on user locations. In terms of physical layer security, measurements were performed in [40], which showed that with RIS deployment, the signal level of an eavesdropper could be reduced down to the noise floor.

Though the above-mentioned studies have largely developed RIS-based free-space models and power-related measurements, unabridged channel observations in practical environment are still rarely reported. Meanwhile, accurate, realistic, yet easy-to-use RIS-empowered channel models are eager to be developed. Undoubtedly, the RIS-assisted cascaded channel exhibits many new propagation characteristics, such as multi-dimensional PL, diversified propagation modes, unpredictable spatial-temporal-frequency properties, etc., which greatly differ from the traditional propagation channels. In consequence, unlike only considering the power gain or simplistically verifying the free-space PL model in existing works, generalizable channel modeling and real channel measurement in practical RIS-related communication scenarios are desired to be fully investigated.

C. Main Contributions

Motivated by such circumstances, in this paper, we conduct multi-scenario broadband¹ channel measurements and channel modeling for RIS-assisted single-input single-output (SISO)

¹Broadband is typically defined as a relative bandwidth within the range of 1% ~ 25% of the center frequency [41]. In our work, the relative bandwidth is $2 \times (2.69 - 2.5) / (2.69 + 2.5) \approx 7\%$.

communications. Considering the dominating role of the sub-6 GHz band serving as the 5G commercial operating frequency band [42], the assessment of RIS-assisted channel at this band will probably be of great significance for its future applications, because of the interoperability between RIS and 5G networks. Thus, we carry out the RIS-assisted channel measurements at the sub-6 GHz licensed frequency band. From multiple perspectives covering frequency, spatial, and temporal domains, we investigate the propagation characteristics of RIS-assisted channels and explain their underlying phenomena. The major contributions are listed as follows.

- We conduct broadband channel measurement campaigns at 2.6 GHz for RIS-assisted NLOS propagation in three scenarios, covering outdoor, indoor, and outdoor-to-indoor (O2I) measurements. Three propagation modes including intelligent reflection with RIS, specular reflection with RIS, and the mode without RIS, are considered in each scenario. In addition, the measured channel data is also compared with the free-space propagation model. The multi-dimensional parameters including Tx-RIS distance, Rx-RIS distance, angle-of-arrival (AoA) onto RIS, and angle-of-departure (AoD) from RIS, etc., are taken into account in our measurement.
- We propose the modified empirical floating-intercept (FI) and close-in (CI) models, to cater for the multi-parameter characteristics of RIS-assisted channels. In comparison to the CI and FI models that we previously proposed in [43], we further refine them from single-dimensional variable to multi-dimensional variables, with distance information as well as angle information included.
- The measurement results are presented and the modeling accuracy is analyzed. From multiple perspectives covering PL gain, PL exponent (PLE), spatial consistency, time dispersion, frequency stationarity, etc., we investigate the characteristics of RIS-assisted channels under different modes as well as in different scenarios. Their underlying propagation phenomena such as the claim of “customizing wireless channels”, are explained and several potential research directions are also pointed out.

D. Organization

The remainder of this paper is outlined as follows. In Section II, the measurement systems and the deployed RIS are described in detail. The measurement scenarios and the measurement procedures are provided in Section III. Then the post-processing of measurement data and the proposed channel models are illustrated in Section IV. In Section V, the measurement results and modeling analyses are presented. Finally, conclusions are drawn and several future works are laid out in Section VI.

II. CHANNEL MEASUREMENT SYSTEMS AND THE DEPLOYED RIS

In this paper, an RIS-assisted SISO communication system is considered, as shown in Fig. 1. The direct channel between Tx and Rx is blocked by obstacles, i.e., a NLOS channel. An RIS is deployed to assist the signal propagation, which is

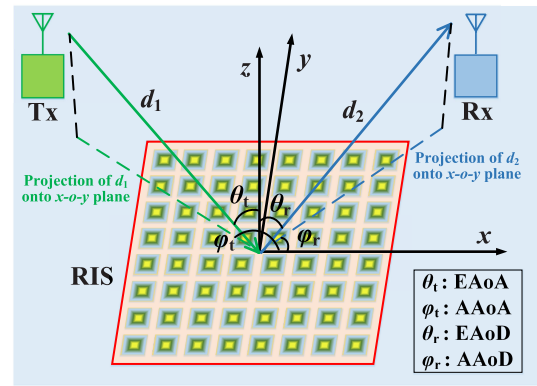


Fig. 1. Parameter definitions for RIS-assisted channel.

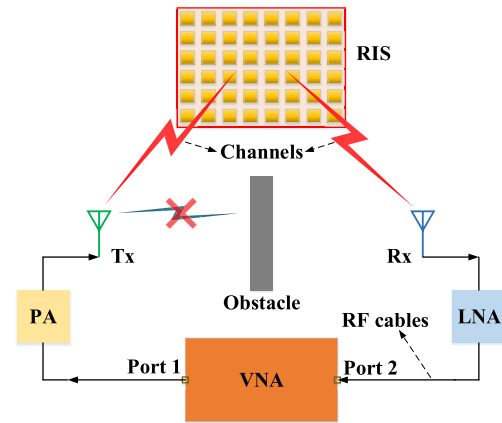


Fig. 2. Descriptions of channel measurement systems.

referred to the RIS-assisted channel with cascaded LOS link in the rest of this paper. The RIS consists of M unit cells per row and N unit cells per column, i.e., $M \times N$ unit cells in total. Each unit cell has a rectangular shape with a horizontal size of d_x and a vertical size of d_y . Moreover, each unit cell has a constant reflection magnitude A and programmable binary discrete phases. Note that the RIS in this paper refers to the family of reflective RIS, by which the signal is neither amplified nor retransmitted. As shown in Fig. 1, let d_1 and d_2 refer to the distances from Tx to the center of RIS and from Rx to the center of RIS, respectively. θ_t , φ_t , θ_r and φ_r respectively indicate the elevation angle-of-arrival (EAoA) and the azimuth angle-of-arrival (AAoA) onto RIS as well as the elevation angle-of-departure (EAoD) and the azimuth angle-of-departure (AAoD) from RIS.

A. Channel Measurement Systems

As shown in Fig. 2, the channel measurement systems are composed of a VNA, a fabricated RIS, a power amplifier (PA), a low noise amplifier (LNA), radio frequency (RF) cables, and two directional horn antennas. In detail, the used VNA version is Agilent N5230C PNA-L. The bandwidth of 190 MHz ranging from 2.5 GHz to 2.69 GHz is selected for the measured broadband signal, which covers the licensed frequency band of current commercial mobile networks [42]. There are 191 scanning points within this measurement bandwidth, with scanning time of $27.3 \mu\text{s}$ for each point by the VNA. As shown

TABLE I
CONFIGURATIONS AND PARAMETERS OF MEASUREMENT SYSTEMS

Configuration	Parameter	Configuration	Parameter
Measurement bandwidth	190 MHz, 2.5 ~ 2.69 GHz	Transmitted power of VNA	10 dBm
Number of frequency scanning points	191	Antenna gain of Tx/Rx	8.25 dBi
Scanning time for one measurement	0.0273 ms \times 191 \approx 5.21 ms	Antenna HPBW of Tx/Rx	60°
Antenna polarization of Tx/Rx	vertical	Loss of RF cables	\leq 0.5 dB/m
PA gain	30 dB	LNA gain	24 dB
Size of RIS	1.6 m \times 0.8 m	Number of unit cell	32 \times 16 = 512
Size of unit cell	0.05 m \times 0.05 m	Phase resolution of unit cell	1-bit
Phase levels of unit cell	{ 55° for coding "0", -125° for coding "1" }	Phase difference of unit cell	180°

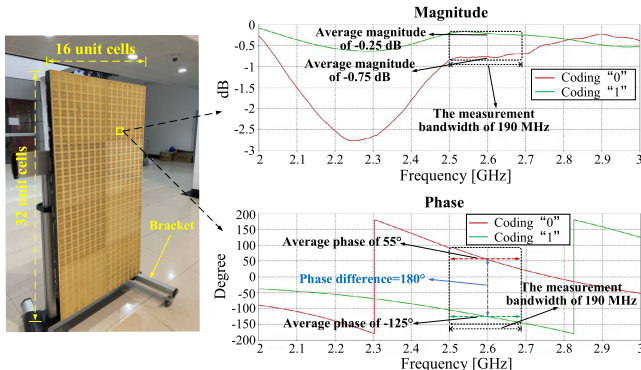


Fig. 3. Image and response characteristics of the deployed RIS.

in Fig. 2, the port 1 of VNA is used to transmit signal and its port 2 receives the signal. Therefore, the scanning data S_{21} is collected as channel transfer function (CTF) in frequency domain. In addition, the antennas used in the measurement system are two wideband double-ridged horn antennas, which serve as Tx and Rx respectively. Each of them is vertically polarized with a gain of 8.25 dBi and has a half power beam width (HPBW) of 60 degrees. The PA connected to Tx has a 30 dB gain and the LNA connected to Rx has a 24 dB gain. The low-loss RF cables with stable amplitude and phase responses are utilized to connect the above equipment. The detailed configurations and parameters of the measurement systems are summarized in Table I.

B. The Deployed RIS

As displayed in Fig. 3, a fabricated RIS with the central operating frequency of 2.6 GHz is utilized for channel measurements. This RIS is composed of 32 unit cells per column and 16 unit cells per row, i.e., 512 unit cells in total, which has a physical size of 1.6 m \times 0.8 m. Each unit cell on the RIS has a square shape of 0.05 m \times 0.05 m, which is nearly half-wavelength of the central operating frequency. A PIN diode is embedded into the unit cell to tune the response characteristics of impinging EM waves. In addition, each unit cell can be independently programmed with 1-bit phase resolution, i.e., two coding states of coding "0" and coding "1", which correspond to the PIN diode being "off" state and "on" state, respectively.

Fig. 3 also shows the magnitude and phase response curves of this RIS with respect to the operating frequency. Within the measurement bandwidth from 2.5 GHz to 2.69 GHz,

the magnitude has an average loss of 0.25 dB for coding "1" and an average loss of 0.75 dB for coding "0", respectively. It is worth mentioning that these losses are much lower than the gain to be provided by RIS beamforming. In addition, within the measurement bandwidth, the phase has an average value of 55° for coding "1" and an average value of -125° for coding "0". Thus, a phase difference of 180° between these two coding states can be achieved.

By pre-designing the coding of each unit cell, this RIS can perform arbitrary beamforming towards desired azimuth and elevation directions. Note that in this paper, the coding schemes of RIS are designed by "**Dynamic Threshold Phase Quantization (DTPQ) method**" in [44]. The idea of DTPQ method is to achieve the maximum phase alignment gain by calculating the RIS discrete phase shift, based on the position relationship of the Tx, Rx and RIS. This method states that by finding the appropriate quantization threshold, which has a computation complexity linear with the number of RIS unit cells, the maximum phase alignment gain can be achieved. This method was proved to be the optimal scheme for RIS discrete phase alignment in free space (See [44] for details). In our measurement campaigns, firstly the parameters d_1 , d_2 , θ_t , φ_t , θ_r and φ_r of the RIS-assisted channels at each point are measured and calculated respectively, according to the geometric position. Based on these parameters, we utilize the "DTPQ method" to generate the codebooks of RIS, which are mapped to each measured point one-to-one. Then, the channel data at each measured point is collected with RIS configuring the corresponding codebook.

III. CHANNEL MEASUREMENT SCENARIOS AND PROCEDURES

In order to comprehensively investigate the propagation characteristics of RIS-assisted channel in practical communications, three typical scenarios including outdoor, indoor, and O2I environments are selected to conduct channel measurement, which cover 2096 channel acquisitions to be measured in total. These measurement scenarios are located at Jiulonghu Campus of Southeast University, in Nanjing, China. The images of channel measurement campaigns in these scenarios are respectively exhibited in Fig. 4. Our measurement campaigns are conducted at night so as to avoid the influences of pedestrians or vehicles on the measurement results. Thus, the measured channels can be viewed as quasi-static.

Aiming to fully reveal the effects of an RIS and its different coding schemes, the channels under three propagation modes

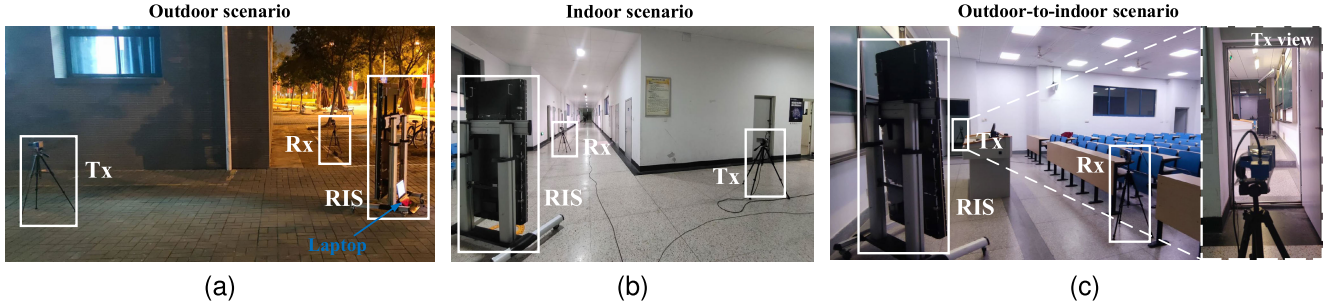


Fig. 4. Images of three channel measurement campaigns. (a) Outdoor scenario. (b) Indoor scenario. (c) O2I scenario.

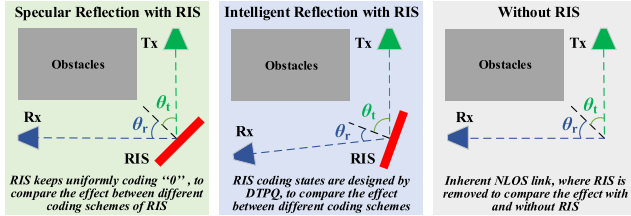


Fig. 5. Schematic diagram of propagation modes.

are measured in each scenario, including *specular reflection with RIS*, *intelligent reflection with RIS*, and *without RIS*, as shown in Fig. 5. In detail, the *specular reflection with RIS* refers to the case that all unit cells of RIS are uniformly configured to be coding “0”, and the RIS does not perform phase regulation dynamically. In this case, the RIS behaves like an equal-sized metal plate [19], which propagates high-quality EM signal only when the Tx and Rx are located at the mirror directions *w.r.t.* the RIS. The *intelligent reflection with RIS* refers to the case that the RIS performs phase regulation dynamically by tuning its phase shifts according to the “DTPQ method” mentioned in Section II-B based on the position relationships of Tx, Rx and RIS, so as to achieve a desired beamforming effect. In this case, the RIS can propagate high-quality EM signal not only when the Tx and Rx are located at the mirror directions *w.r.t.* the RIS, but also when they are located at other directions. By contrast, the mode *without RIS* refers to the case that the RIS is removed from the transmission environment. Thus, in this case, the propagation mode is dominated by the inherent NLOS link. The detailed information on measurement scenarios and procedures is provided in the subsequent subsections.

A. Outdoor Channel Measurement

For outdoor measurement, the building corner next to Teaching Building No. 8 outdoors is selected as measurement site. The scenario and procedure for this measurement are exhibited in Fig. 6. In this figure, the communication links between two sides of this building suffer from NLOS propagation, due to the blockage by the exterior wall of building. The exterior facades of this building are fully covered by concretes. Two horn antennas serving as Tx and Rx, are respectively placed at the east-side and south-side spaces of the building.

From Fig. 6, Tx is kept at a perpendicular distance of 1.5 m from the east facades of building, and moves along the line (referred to as “Tx trajectory line”) parallel to the

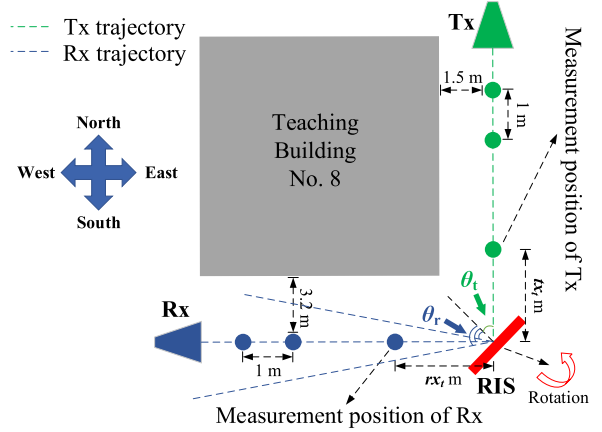


Fig. 6. Scenario and procedure for outdoor measurement.

east facades. In addition, Rx is kept at a perpendicular distance of 3.2 m from the south facades of building, and moves along the line (referred to as “Rx trajectory line”) parallel to the south facades. The RIS is positioned at the intersection of Tx and Rx trajectory lines. Throughout this measurement, both Tx and Rx maintain facing the RIS.

Tx is initially placed at a distance of tx_t m from RIS and moves away from RIS at a step of 1 m along the Tx trajectory line, until the Tx-RIS distance reaches tx_p m. Similarly, Rx is initially placed at a distance of rx_t m from the RIS and moves away from RIS at a step of 1 m along the Rx trajectory line, until the Rx-RIS distance reaches rx_p m. Note that in this measurement, Tx, Rx, and the center of RIS are fixed to be at the same height of 1 m above the ground. According to Fig. 1, the y -axis is used to model the heights of Tx, Rx, and RIS. Thus, Tx and Rx are located at the x - z plane when they are at the same height with the center of RIS, resulting in the AAoA $\varphi_t = 180^\circ$ and the AAoD $\varphi_r = 0^\circ$.

In outdoor measurement, for specular reflection with RIS, the RIS is fixed at $\theta_t = 45^\circ$ and $\theta_r = 45^\circ$. tx_t , tx_p , rx_t , and rx_p are 5 m, 18 m, 5 m, and 18 m, respectively. For intelligent reflection with RIS, the RIS is appropriately rotated to form 9 different pairs of EAoA θ_t and EAoD θ_r , i.e., $\theta_t \in \{45^\circ, 60^\circ, 75^\circ\}$ and $\theta_r \in \{30^\circ, 45^\circ, 60^\circ\}$, as illustrated in Fig. 6. For the mode without RIS, the RIS is removed. Thus, there are a virtual EAoA $\theta_t = 45^\circ$ and a virtual EAoD $\theta_r = 45^\circ$. tx_t , tx_p , rx_t , and rx_p are 5 m, 18 m, 5 m, and 18 m, respectively. These three modes include 196, 866, and 196 points to be measured respectively. The detailed

TABLE II
MEASUREMENT PARAMETERS OF OUTDOOR SCENARIO

Propagation mode	Without RIS	Specular reflection with RIS	Intelligent reflection with RIS								
			Case 1	Case 2	Case 3	Case 4	Case 5	Case 6	Case 7	Case 8	Case 9
EAoA θ_t	45°	45°	45°	45°	45°	60°	60°	60°	75°	75°	75°
EAoD θ_r	45°	45°	30°	45°	60°	30°	45°	60°	30°	45°	60°
tx_t (m)	5	5	9	5	9	9	9	9	9	9	9
tx_p (m)	18	18	18	18	18	18	18	18	18	18	18
rx_t (m)	5	5	5	5	8	8	8	8	8	8	8
rx_p (m)	18	18	12	18	15	18	15	15	15	15	15
Number of Tx points	14	14	10	14	10	10	10	10	10	10	10
Number of Rx points	14	14	8	14	8	11	8	8	8	8	8
Number of total points	14 × 14 = 196	14 × 14 = 196	10 × 8 + 14 × 14 + 10 × 8 + 10 × 11 + 10 × 8 + 10 × 8 + 10 × 8 + 10 × 8 = 866								

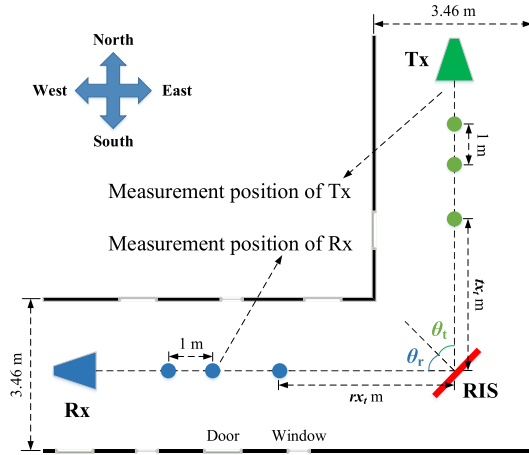


Fig. 7. Scenario and procedure for indoor measurement.

configurations on the outdoor measurement are parameterized in Table II.

B. Indoor Channel Measurement

For indoor measurement, the corridor on the first floor of Teaching Building No. 2, which is next to the Liangjiang Road, is selected as measurement site. The measurement scenario and procedure are shown in Fig. 7. From this figure, an inherent NLOS transmission link exists, due to the fact that both sides of the corridor are perpendicular to each other. The walls of this corridor are covered with concrete, among which the aluminum alloy doors and several glazed windows are embedded. The corridor has a width of 3.46 m and a height of 3.32 m. The south-north corridor and the east-west corridor are respectively selected to place Tx and Rx.

As shown in Fig. 7, Tx moves along the central axis of south-north corridor (referred to as “Tx trajectory line”) and Rx moves along the central axis of east-west corridor (referred to as “Rx trajectory line”). The RIS is positioned at the intersection of Tx and Rx trajectory lines. Two horn antennas serving as Tx and Rx are respectively placed facing the RIS throughout this measurement. Tx is initially placed at a distance of tx_t m from RIS and moves away from RIS at a step of 1 m along the Tx trajectory line, until the Tx-RIS

TABLE III
MEASUREMENT PARAMETERS OF INDOOR SCENARIO

Propagation mode	Without RIS	Specular reflection with RIS	Intelligent reflection with RIS	
			Case 1	Case 2
EAoA θ_t	45°	45°	45°	60°
EAoD θ_r	45°	45°	45°	30°
tx_t (m)	5	5	5	5
tx_p (m)	18	18	18	18
rx_t (m)	5	5	5	5
rx_p (m)	18	18	18	18
Number of Tx points	14	14	14	14
Number of Rx points	14	14	14	14
Number of total points	14 × 14 = 196	14 × 14 = 196	14 × 14 + 14 × 14 = 392	

distance reaches tx_p m. Similar with the outdoor scenario, Rx is initially placed at a distance of rx_t m from the RIS and moves away from RIS at a step of 1 m along the Rx trajectory line, until the Rx-RIS distance reaches rx_p m. In this measurement, Tx, Rx, and the center of RIS are also fixed to be at the same height of 1 m above the ground, thus the AAoA $\varphi_t = 180^\circ$ and the AAoD $\varphi_r = 0^\circ$.

In this measurement, three propagation modes as in the outdoor scenario, including *specular reflection with RIS*, *intelligent reflection with RIS*, and *without RIS*, are also measured. For specular reflection with RIS, the RIS is fixed at $\theta_t = 45^\circ$ and $\theta_r = 45^\circ$. Meanwhile, tx_t , tx_p , rx_t , and rx_p are 5 m, 18 m, 5 m, and 18 m, respectively. For intelligent reflection with RIS, the RIS is appropriately rotated to form 2 different pairs of θ_t and θ_r , i.e., $\theta_t = 45^\circ$, $\theta_r = 45^\circ$ and $\theta_t = 60^\circ$, $\theta_r = 30^\circ$, as illustrated in Fig. 7. For the mode without RIS, measurement settings are the same with the corresponding mode in the outdoor scenario. These three modes contain 196, 392, and 196 points to be measured respectively. The detailed configurations of this measurement are summarized in Table III.

C. O2I Channel Measurement

For O2I measurement, the classroom on the first floor of Teaching Building No. 7, is selected as measurement site. The scenario and procedure for this measurement are exhibited

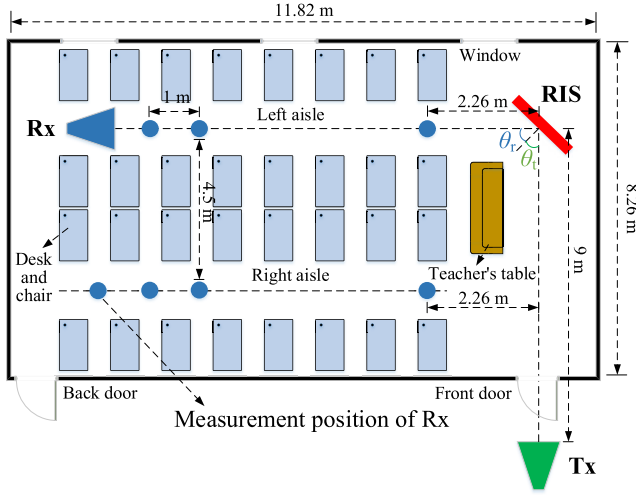


Fig. 8. Scenario and procedure for O2I measurement.

in Fig. 8. In this scenario, Rx in the classroom is weakly covered by communication signals when Tx locates outside the classroom, due to the blockage by concrete walls between Tx and Rx. Thus, their communication links can be reasonably considered as NLOS. This measured classroom has a width of 8.26 m, a length of 11.82 m, and a height of 3.32 m. It is surrounded by concrete walls, where several glazed windows and two aluminum alloy doors are embedded into the walls. In addition, this classroom is typically filled with a number of orderly-arranged desks and chairs, as well as a teacher's table. There are two aisles in the classroom, as shown in Fig. 8.

In this measurement, Tx is fixed outside the classroom and faces the front door, which is kept open all along. The RIS is positioned at the intersection of the Tx-front door line and the left aisle, with a distance of 9 m away from Tx and $\theta_t = 45^\circ$. Two horn antennas serving as Tx and Rx maintain facing the RIS throughout this measurement. Similar with the outdoor and indoor scenarios, in this measurement, Tx, Rx, and the center of RIS are also fixed to be at the same height of 1 m above the ground, thus the EAoA $\varphi_t = 180^\circ$ and the EAoD $\varphi_r = 0^\circ$. Rx moves along these two aisles, respectively. In left aisle, $\theta_r = 45^\circ$ can be readily determined at each measured point. Rx is initially placed at a distance of $rx_t = 2.26$ m from RIS and moves away from RIS at a step of 1 m, until the final distance reaches $rx_p = 10.26$ m. In right aisle, Rx is initially positioned at a perpendicular distance of $rx_t = 2.26$ m to the Tx-RIS line, and moves away from this line at a step of 1 m, until the final distance reaches $rx_p = 10.26$ m. Based on geometric relationships, the EAoD θ_r^i at the i th point in right aisle can be expressed as

$$\theta_r^i = \arctan\left(\frac{2.26 + (i-1) \times 1}{4.5}\right) - \left(\frac{\pi}{2} - \theta_t\right). \quad (1)$$

Then we obtain the EAoD set $\mathcal{R} = \{-18.33^\circ, -9.08^\circ, -1.57^\circ, 4.45^\circ, 9.29^\circ, 13.2^\circ, 16.42^\circ, 19.08^\circ, 21.32^\circ\}$ in the order of positions 1~9 in right aisle.

In this measurement, three propagation modes, i.e., *specular reflection with RIS*, *intelligent reflection with RIS*, and *without RIS*, are also measured. The detailed configurations on these

TABLE IV
MEASUREMENT PARAMETERS OF O2I SCENARIO

Propagation mode	Without RIS		Specular reflection with RIS		Intelligent reflection with RIS	
	Left aisle	Right aisle ¹	Left aisle	Right aisle ¹	Left aisle	Right aisle ¹
EAoA θ_t	45°	45°	45°	45°	45°	45°
EAoD θ_r	45°	\mathcal{R}	45°	\mathcal{R}	45°	\mathcal{R}
d_1 (m)	9	9	9	9	9	9
rx_t (m)	2.26	2.26	2.26	2.26	2.26	2.26
rx_p (m)	10.26	10.26	10.26	10.26	10.26	10.26
Number of Rx points	9	9	9	9	9	9
Number of total points	9 + 9 = 18		9 + 9 = 18		9 + 9 = 18	

¹ For three propagation modes, rx_t and rx_p in right aisle in Table IV refer to the perpendicular distances from Rx to Tx-RIS line.

three modes are summarized in Table IV. The coding schemes of RIS under each mode are the same as the corresponding ones in the outdoor and indoor scenarios. For each mode in this measurement, 18 points are measured.

IV. DATA POST-PROCESSING AND CHANNEL MODELING

In this section, the post-processing of measurement data including PL, PDP, root mean square delay spread (RMS DS), etc., are introduced. In addition, based on the traditionally-used FI and CI models, two empirical channel models for RIS-assisted channel covering distance information and angle information are proposed.

A. Measurement Data Post-Processing

For the sake of illustration, the signals transmitted from port 1 of VNA and received at port 2 of VNA in frequency domain are denoted as $X(f)$ and $Y(f)$ respectively. The Tx antenna response, Rx antenna response, measurement system response and channel response are respectively represented as $G_t(f)$, $G_r(f)$, $G(f)$ and $H(f)$. The collected data by VNA is denoted as $H_V(f)$, which can be calculated by

$$H_V(f) = S_{21}(f) = \frac{Y(f)}{X(f)} = G_t(f)G_r(f)G(f)H(f). \quad (2)$$

Then, the back-to-back calibration is performed. During the calibration, the components of the measurement systems in Fig. 2 except for the antennas, are connected directly together to obtain the system response $G(f)$. Subsequently, the antenna responses $G_t(f)$ and $G_r(f)$ are measured respectively in anechoic chamber, which are 8.25 dBi at the measured bandwidth. After that, the channel response in frequency domain can be calculated by

$$H(f) = \frac{H_V(f)}{G_t(f)G_r(f)G(f)}. \quad (3)$$

The measured PL in logarithmic scale is calculated by

$$PL = 10 \times \log_{10} \left(\frac{\sum_{k=1}^K (|H_k(f)|^2)}{K} \right), \quad (4)$$

where $H_k(f)$ denotes the channel response of the k th frequency scanning point, $K = 191$ is the number of frequency

scanning points. Then, the channel impulse response (CIR) in temporal domain is determined by inverse Fourier transform,

$$h(t, \tau) = \text{IFT}(H(f) \times W_{\text{hann}}), \quad (5)$$

where $\text{IFT}(\cdot)$ denotes the inverse Fourier transform operation, W_{hann} represents the Hanning-window. Then, the power delay profile (PDP) is calculated by

$$PDP = |h(t, \tau)|^2. \quad (6)$$

In this paper, the multi-path components (MPCs) of PDP above the detection threshold P_{th} are considered valid, and otherwise the MPCs are deemed outliers and discarded. The detection threshold P_{th} can be determined by (7) [45].

$$P_{th} = \max(P_{\max} - \gamma_P, N_0 + \gamma_N), \quad (7)$$

where P_{\max} is the maximum peak power of PDP, γ_P is the power threshold relative to the maximum peak, N_0 is the noise floor of PDP, γ_N is the power threshold relative to the noise floor. In this paper, γ_P and γ_N are set to 60 dB and 15 dB, respectively.

For describing the channel shape in temporal domain, RMS DS can be represented as

$$\tau_{\text{RMS}} = \sqrt{\frac{\sum_{l=1}^L P_l \tau_l^2}{\sum_{l=1}^L P_l} - \left(\frac{\sum_{l=1}^L P_l \tau_l}{\sum_{l=1}^L P_l} \right)^2}, \quad (8)$$

where L is the number of the valid MPCs in PDP, τ_l denotes the delay of the l th valid MPC calculated by $\tau_l = (l-1)\Delta_\tau$, Δ_τ denotes the delay resolution equaling to the inverse of the measured signal bandwidth, and P_l denotes the power of the l th valid MPC.

B. Channel Modeling

In this subsection, the modeling methods for RIS-assisted channels are investigated. In the existing channel-related work, the FI model has been adopted widely to describe the characteristics of PL in the 3rd Generation Partnership Project (3GPP) and International Telecommunication Union (ITU) standards [46], [47]. Meanwhile, though the CI model only focuses on the PLE, it still attracts great attention due to its model parameter stability and intuitive perspective. In [43], we have proposed the applicable FI and CI models to RIS-assisted channel. Nevertheless, these two models in [43] only considered the single-dimensional variable, i.e., the Rx-RIS distance, which limited their generalizations applied in various scenarios. Thus, in this paper, we further refine them from single-dimensional variable to multi-dimensional variables. The modified FI and CI models are proposed for general RIS-assisted channels, which include distance information and angle information.

For the convenience of presentation, the traditional FI model is provided as follows.

$$PL_{FI} = \alpha + 10\beta \log_{10}(d) + X_\sigma^{FI}, \quad (9)$$

where d (m) is the 3D direct distance between Tx and Rx, β is the PLE related to the variation of distance, α is intercept parameter associated with the offset value of PL, X_σ^{FI} is

shadow factor (SF) for describing the fitting deviation, which is usually modeled as Gaussian distribution $\mathcal{N}(\mu, \sigma^2)$ [45].

The traditional CI model can be expressed as

$$PL_{CI} = PL_{FS}(d_0) + 10n \log_{10}\left(\frac{d}{d_0}\right) + X_\sigma^{CI}, \quad (10)$$

where n is the PLE associated with the variation of distance d , d_0 is the reference distance, which is usually set to 1 m, $PL_{FS}(d_0)$ is the PL at reference distance d_0 in free space, and X_σ^{CI} is SF following Gaussian distribution $\mathcal{N}(\mu, \sigma^2)$.

As we can see, both of the traditional FI and CI models focus on the PL fittings under one-dimensional variable (i.e., d). However, for RIS-assisted channel, there are multi-dimensional variables, e.g., d_1 , d_2 , θ_t , θ_r , etc., to be involved in channel modeling. The theoretical RIS-assisted channel models in free space were proposed in [19], which can be expressed as

$$PL_{FS}^{RIS} = \frac{16\pi^2(d_1 d_2)^2}{G_t(f)G_r(f)(MN d_x d_y)^2 \cos(\theta_t) \cos(\theta_r) A^2}, \quad (11)$$

where A is the reflection magnitude of each unit cell, $\cos(\theta_t)$ and $\cos(\theta_r)$ denote the normalized power radiation patterns of emission and reception for each unit cell, whose accuracy in characterizing the behavior of each unit cell has been evidenced in [19]. (11) indicates that the PL in angle domain is only related to θ_t and θ_r , and is irrelevant to φ_t and φ_r in Fig. 1. From this equation, it can be readily derived that, in free space, the PLEs on d_1 and d_2 are 2 and the PLEs on $\cos(\theta_t)$ and $\cos(\theta_r)$ are -1 in logarithmic scale, respectively. As a consequence, the traditional FI and CI models should be deformed to adapt to the multi-dimensional variables of RIS-assisted channel.

In this paper, we propose the modified FI and CI models for the PL of RIS-assisted channel, as expressed in (12) and (13), as shown at the bottom of the next page, respectively. In (12), β_1 and β_2 are the PLEs to describe the dependence of PL on d_1 and d_2 , λ_1 and λ_2 are the PLEs to indicate the dependence of PL on θ_t and θ_r , α denotes the intercept parameter associated with the offset value of PL. X_σ^{FI} denotes SF, which is modeled as Gaussian distribution $\mathcal{N}(\mu, \sigma^2)$. In (13), n_1 and n_2 are the PLEs to describe the dependence of PL on d_1 and d_2 , μ_1 and μ_2 are the PLEs to indicate the dependence of PL on θ_t and θ_r , X_σ^{CI} is SF following the Gaussian distribution $\mathcal{N}(\mu, \sigma^2)$, d_0^1 , d_0^2 , θ_0^t , and θ_0^r denote the reference distances of d_1 and d_2 as well as the reference angles of θ_t and θ_r , respectively. In this paper, d_0^1 , d_0^2 , θ_0^t , and θ_0^r are set to 1 m, 1 m, 0° , and 0° respectively, whereas these reference values can be adjusted appropriately in each scenario where applicable. Moreover, $PL_{FS}^{RIS}(d_0^1, d_0^2, \theta_0^t, \theta_0^r)$ represents the PL with these reference variables in free space, which is calculated to be 21.38 dB according to (11). Then, a simplified expression of (13) can be written as (14), as shown at the bottom of the next page.

The detailed comparisons of the modified and traditional FI and CI models as well as PL model proposed in [19] are summarized in Table V. It should be noted that the effects of the size, number, and reflection magnitude of unit cells

TABLE V
COMPARISONS OF PL MODELS

Models	Variables	Fitting factors	Properties	Applicable ranges
Traditional FI	d	α, β	empirical	Traditional point-to-point communications
Traditional CI	d	n	empirical	Traditional point-to-point communications
PL model in [19]	$d_1, d_2, \theta_t, \theta_r$	—	deterministic	Free-space RIS-assisted communications
Modified FI	$d_1, d_2, \theta_t, \theta_r$	$\alpha, \beta_1, \beta_2, \lambda_1, \lambda_2$	empirical	Practical RIS-assisted communications
Modified CI	$d_1, d_2, \theta_t, \theta_r$	n_1, n_2, μ_1, μ_2	empirical	Practical RIS-assisted communications

on PL, are integrated into the term of $PL_{FS}^{RIS}(d_0^1, d_0^2, \theta_0^t, \theta_0^r)$ in the modified CI model. The value of $PL_{FS}^{RIS}(d_0^1, d_0^2, \theta_0^t, \theta_0^r)$ indicates the dependence of PL on these factors, which can be calculated by (11). In addition, in the modified FI model, the dependence of PL on these factors is described by the value of α , which can be calculated through the fitting process.

In this paper, the least square (LS) method is utilized to fit the measurement data with the modified FI and CI models, respectively. In detail, LS method adopts Levenberg-marquardt algorithm, which requires presetting the upper and lower bounds of the parameters to be fitted. In this paper, the upper and lower bounds are set to (50, 3, 3, 2, 2) and (10, 1, 1, 0, 0) respectively, for the parameters ($\alpha, \beta_1, \beta_2, \lambda_1, \lambda_2$) in the modified FI model. Moreover, the upper and lower bounds are set to (21.38, 3, 3, 2, 2) and (21.38, 1, 1, 0, 0) respectively, for the parameters ($PL_{FS}^{RIS}, n_1, n_2, \mu_1, \mu_2$) in the modified CI model.

V. MEASUREMENT RESULTS AND MODELING ANALYSES

In this section, the measured channel data in three measurement campaigns is presented. The modified CI and FI models are fitted with the measured channel data under *intelligent reflection with RIS*, which are also compared with the free-space channel model proposed in [19]. Moreover, the channel characteristics in temporal, frequency, and spatial domains including PDP, RMS DS, frequency stationarity, spatial consistency, etc., are analyzed and explained.

A. Outdoor Measurement

For the mode of intelligent reflection with RIS in outdoor measurement, the fitting results of the modified CI and FI models with measurement data as well as free-space data are summarized in Table VI. From Table VI, it can be found that for both of the modified CI and FI models, the fitted

TABLE VI
FITTING RESULTS FOR OUTDOOR MEASUREMENT

Parameters	α (PL_{FS}^{RIS})	β_1 (n_1)	β_2 (n_2)	λ_1 (μ_1)	λ_2 (μ_2)
Modified FI with measurement data	20.08	2.29	1.88	1.21	0.65
Modified FI with free-space data	24.52	2.05	1.95	1.15	0.79
Modified CI with measurement data	21.38	2.22	1.82	1.21	0.64
Modified CI with free-space data	21.38	2.21	2.08	1.14	0.81

PLE on d_1 with free-space data is slightly lower than that with measurement data. On the contrary, the fitted PLE on d_2 with free-space data is slightly higher than that with measurement data. In addition, similar phenomena can be seen in angle domain that the fitted PLEs on θ_t and on θ_r with free-space data are respectively lower and higher than those with measurement data. These phenomena may result from that in outdoor measurement, Rx positions are surrounded by abundant scatterers such as neighbouring buildings while Tx positions are next to open streets.

Fig. 9 depicts the modified CI and FI models fitted with the measurement data under $\theta_t = 75^\circ$ and $\theta_r = 60^\circ$. It can be visually observed that both of the proposed models fit well with the measurement data. Fig. 10 exhibits the cumulative distribution functions (CDFs) of SFs for the modified FI and CI models as well as the PL model in [19], which are fitted with Gaussian distributions. Herein, X_σ^{FI} , X_σ^{CI} and X_σ^{th} denote the differences between the measured PL and the predicted PLs of these three models, respectively. From this figure, the modified FI and CI models have low mean values of -0.06 dB and 0.05 dB respectively, with the same standard deviation of 2.53 dB, which illustrate their high prediction

$$PL_{FI}^{RIS}(d_1, d_2, \theta_t, \theta_r) = \alpha + 10\beta_1 \log_{10}(d_1) + 10\beta_2 \log_{10}(d_2) - 10\lambda_1 \log_{10}(\cos(\theta_t)) - 10\lambda_2 \log_{10}(\cos(\theta_r)) + X_\sigma^{FI}. \quad (12)$$

$$PL_{CI}^{RIS}(d_1, d_2, \theta_t, \theta_r) = PL_{FS}^{RIS}(d_0^1, d_0^2, \theta_0^t, \theta_0^r) + 10n_1 \log_{10}\left(\frac{d_1}{d_0^1}\right) + 10n_2 \log_{10}\left(\frac{d_2}{d_0^2}\right) - 10\mu_1 \log_{10}\left(\frac{\cos(\theta_t)}{\cos(\theta_0^t)}\right) - 10\mu_2 \log_{10}\left(\frac{\cos(\theta_r)}{\cos(\theta_0^r)}\right) + X_\sigma^{CI}. \quad (13)$$

$$PL_{CI}^{RIS}(d_1, d_2, \theta_t, \theta_r) = 21.38 + 10n_1 \log_{10}(d_1) + 10n_2 \log_{10}(d_2) - 10\mu_1 \log_{10}(\cos(\theta_t)) - 10\mu_2 \log_{10}(\cos(\theta_r)) + X_\sigma^{CI}. \quad (14)$$

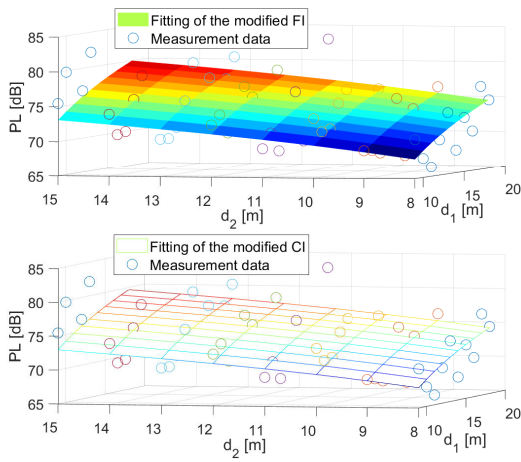


Fig. 9. The modified models with measurement data.

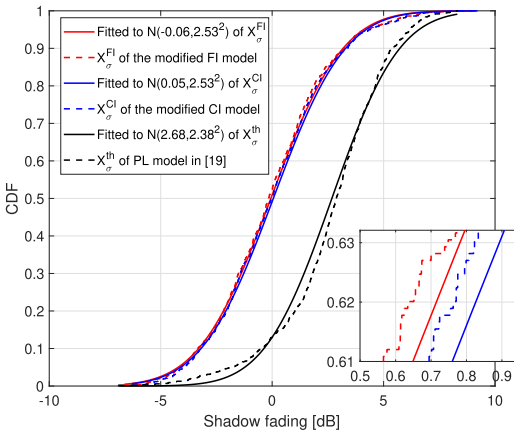


Fig. 10. SFs and the fitted CDFs.

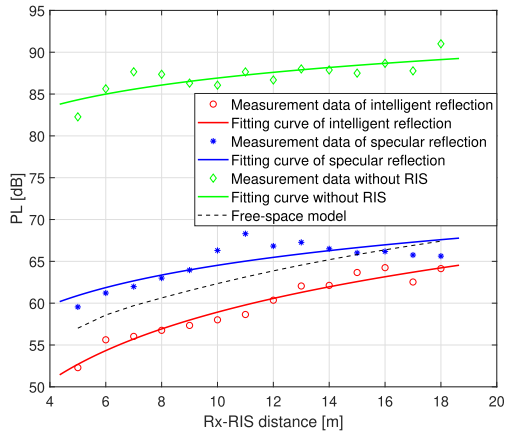
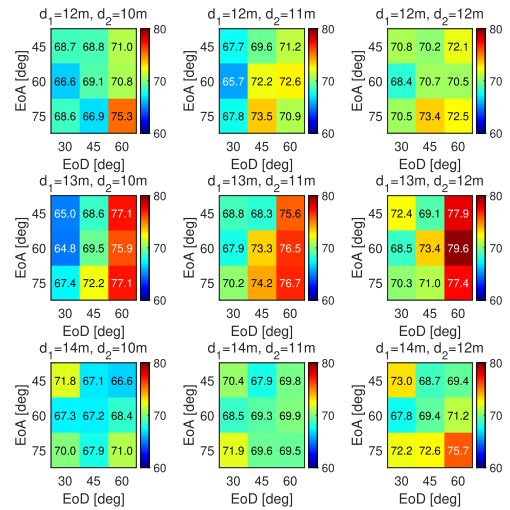


Fig. 11. PLs of measurement data and free-space data.

accuracy on PL. Nevertheless, the mean value for PL model in [19] is relatively high, i.e., 2.68 dB, indicating the large discrepancy between its predicted PL and the measured PL.

Fig. 11 provides the measured PL for three modes in outdoor scenario as well as the free-space PL, under $\theta_t = 45^\circ$, $\theta_r = 45^\circ$, and $d_1 = 6$ m. Note that in Fig. 11, the PL *without RIS* is also influenced by the Rx-RIS distance. This is because, for this mode the horizontal axis, i.e., the Rx-RIS distance, represents the distance between Rx and the

Fig. 12. PLs under $d_1 = 12 \sim 14$ m and $d_2 = 10 \sim 12$ m.

point where RIS is located in the other two modes, so as to compare the differences between the three modes. From this figure, the PLE for intelligent reflection mode shows a similar value as the free-space model. Nevertheless, there is a small gap of about 3 dB between the predicted PL by [19] and the measured PL. In addition, thanks to the capability of focusing signal energy for intelligent reflection mode, its PL demonstrates a maximum gain of 9.7 dB than that for specular reflection mode and a maximum gain of 30 dB than that without RIS, respectively. As d_2 increases, the PL difference between the intelligent and specular reflection modes becomes smaller. When d_2 is large enough, their PLs tend to coincide. This shows that when $\theta_t = \theta_r$, the beamforming schemes of *specular/intelligent reflection with RIS* behave similarly in the case of extremely far field. It can be explained by the fact that the *specular reflection with RIS* scatters EM signals towards all directions in the near field.² But in the far field, such diffuse scattering gets weaker and beamforming towards the mirror direction is more inclined to perform.

Fig. 12 illustrates the PLs vs EoA and EoD under $d_1 = 12 \sim 14$ m and $d_2 = 10 \sim 12$ m for intelligent reflection mode, with color coded against PL. From this figure, the PL keeps up the trend of increasing as EoA and EoD become larger, despite a slight fluctuation. This phenomenon is well consistent with the theoretical PL scaling law in angle domain described in [18], and [19].

Fig. 13 demonstrates the PDP comparison of three modes under $\theta_t = 45^\circ$, $\theta_r = 45^\circ$, $d_1 = 9$ m, and $d_2 = 8$ m. From this figure, the PDP peak of intelligent reflection mode is highest, followed by that of specular reflection mode, and the PDP peak without RIS is lowest due to its inherent NLOS propagation. Moreover, the delays on PDP peaks of intelligent

²Presently, there is no unified definition on the boundary between the near and far fields of the RIS. According to the classical Rayleigh distance criterion [17], which is widely used to calculate the boundaries of large-scale antenna arrays, the boundary distance is 55.45 m in our measured scenarios. According to Eq. (19) in [18], which assumes either Tx or Rx is located in extremely far field, the boundary distance is calculated to be 10.21 m in our measured scenarios. Thus, the measurement environment involved in this paper is roughly considered as near field or transition field between the near and far fields of the RIS.

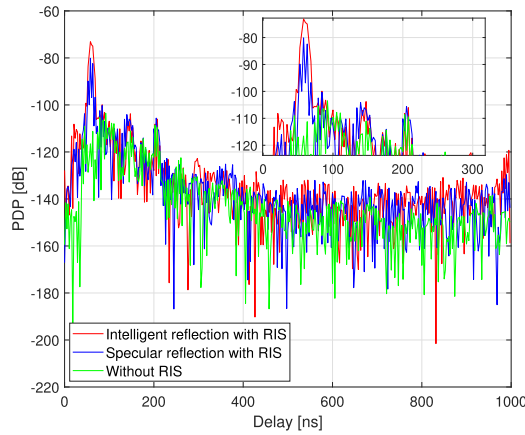


Fig. 13. PDP comparison of three modes.

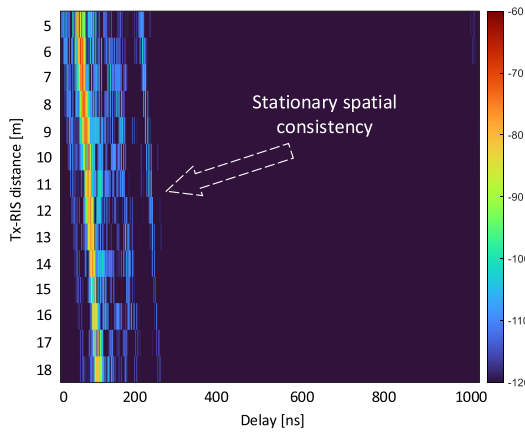


Fig. 14. PDP evolution vs delay and position.

and specular reflection modes are almost the same, which are lower than that without RIS. This can be explained by the fact that the signal propagation without RIS is dominated by the scattering and diffraction aroused from the surroundings, such as the walls, trees, and bicycles. Compared to the RIS cascade channels, these scattering and diffraction have longer propagation distances, which result in larger excess delays. From the field-of-view of Rx, Fig. 14 illustrates the PDP evolution vs d_1 and delay for intelligent reflection mode, which are linked across positions, under $d_2 = 8$ m, $\theta_t = 45^\circ$, $\theta_r = 45^\circ$. It indicates a well stationary spatial consistency on MPC evolution when Tx is moved in our measurement.

Fig. 15 shows the RMS DSs for three modes and the fitted Gaussian distributions $\mathcal{N}(\mu, \sigma^2)$, under $\theta_t = 45^\circ$ and $\theta_r = 45^\circ$. The means of these CDFs are 8.42 ns, 10.79 ns and 37.55 ns respectively for the modes of intelligent reflection, specular reflection and without RIS, as displayed in Table VII. The higher μ represents the more diffuse multi-path distribution. This phenomenon illustrates that the channel time dispersion of intelligent reflection mode is lower than that of specular reflection mode, and the channel time dispersion without RIS is the strongest. This results from that RMS DS is a metric to evaluate the degree of multi-path dispersion. Firstly, the intelligent reflection mode enables focusing signal energy towards a desired direction by beamforming, which weakens

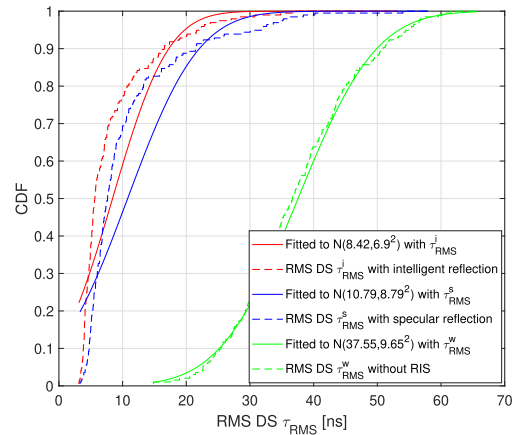


Fig. 15. RMS DSs for three modes.

TABLE VII
FITTED DISTRIBUTIONS OF RMS DSs

Scenarios	Without RIS		Specular reflection		Intelligent reflection	
	μ [ns]	σ [ns]	μ [ns]	σ [ns]	μ [ns]	σ [ns]
Outdoor	37.55	9.65	10.79	8.79	8.42	6.9
Indoor	13.04	4.29	5.88	4.31	5.01	2.74
OZI	24.21	8.2	16.04	9.69	10.36	9.53

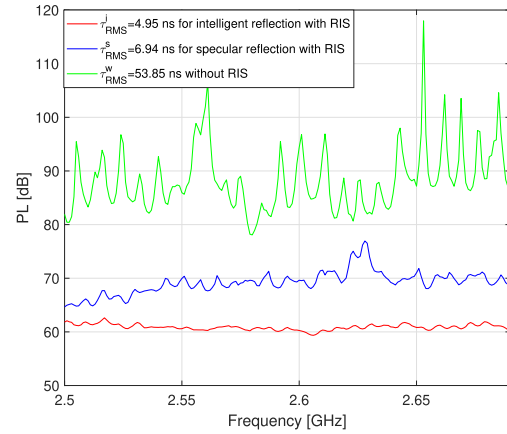


Fig. 16. Frequency stationarity for three modes.

the multi-path dispersion. Secondly, the specular reflection mode may scatter EM signals towards undesired directions, which contributes to a stronger multi-path dispersion than intelligent reflection mode. Finally, the mode without RIS is dominated by scattering, diffraction, and diffuse reflection, whose multi-path effect is the richest. These phenomena and explanations are consistent with the observations in Fig. 13.

Fig. 16 demonstrates the frequency stationarity within the measured bandwidth for the three considered modes under $\theta_t = 45^\circ$, $\theta_r = 45^\circ$, $d_1 = 10$ m and $d_2 = 10$ m. Frequency stationarity is closely related to the richness of multi-path. From this figure, the propagation signal without RIS shows the strongest frequency selective fading, due to the fact that its dominant propagation (scattering, diffraction, and diffuse reflection) is comprised of abundant MPCs. In addition, the propagation signal for specular reflection with RIS demonstrates a slight but non-negligible frequency selective fading,

TABLE VIII
FITTING RESULTS FOR INDOOR MEASUREMENT

Parameters	α (PL_{FIS}^{RIS})	β_1 (n_1)	β_2 (n_2)
Modified FI with measurement data	28.16	1.9	1.68
Modified FI with free-space data	28.7	1.96	1.96
Modified CI with measurement data	26.97	1.95	1.74
Modified CI with free-space data	26.97	2.04	2.04

which evidences that this mode still generates the additional diffuse MPCs even when RIS is orienting signal towards the mirror directions. By contrast, the intelligent reflection with RIS has a nearly flat fading environment, illuminating its significant beamforming capability without creating excrescent MPCs. These phenomena can also be explained by a formulaic relationship of the coherence bandwidth B_c , signal bandwidth B_s and frequency selectivity Δ , as (15).

$$\Delta \propto B_c/B_s. \quad (15)$$

(15) states that the frequency selectivity is proportional to the ratio of coherence bandwidth to signal bandwidth. The coherence bandwidth is inversely proportional to its RMS DS:

$$B_c \propto 1/\tau_{RMS}. \quad (16)$$

Therefore, given the fixed signal bandwidth, the frequency selectivity is inversely proportional to its RMS DS:

$$\Delta \propto 1/(B_s \tau_{RMS}). \quad (17)$$

From Fig. 16, the RMS DSs of the intelligent reflection with RIS, specular reflection with RIS, and the mode without RIS are 4.95 ns, 6.94 ns, and 53.85 ns, respectively. Following (17), their frequency selectivity gets stronger by this order.

B. Indoor Measurement

For the mode of intelligent reflection with RIS in indoor measurement, the fitting results of the modified CI and FI models with the measured data as well as the free-space data are summarized in Table VIII. Note that in this measurement, the EAoA and EAoD are fixed to be 45° , thus λ_1 (μ_1) and λ_2 (μ_2) of the modified FI (CI) model are not taken into account. The reference value $PL_{FIS}^{RIS} = 26.97$ dB of the modified CI model is calculated under $\theta_t = 45^\circ$, $\theta_r = 45^\circ$, $d_1 = 1$ m, and $d_2 = 1$ m. From this table, it can be found that for both of the modified CI and FI models, the fitted PLEs on d_1 and d_2 with free-space data are slightly higher than those with measurement data. This can be explained by that in indoor corridor scenario, there exists a non-ignorable wave-guide effect, which results in the lower PLEs.

Similar to Fig. 10, Fig. 17 exhibits the CDFs of SFs for the modified FI and CI models as well as the PL model in [19], where X_σ^{FI} , X_σ^{CI} and X_σ^{th} denote the same meanings as in outdoor measurement. In Fig. 17, the modified FI and CI models have low mean values of 0.01 dB and 0.07 dB respectively, with the same standard deviation of 2.46 dB,

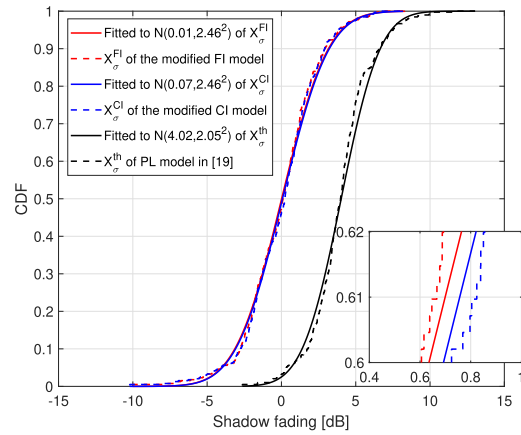


Fig. 17. SFs and the fitted CDFs.

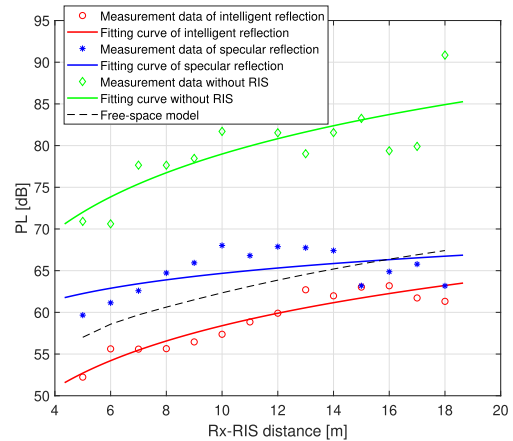


Fig. 18. PLs of measurement data and free-space data.

indicating their high and similar prediction accuracy on PL. Similar to the outdoor scenario, the mean value for PL model in [19] is prominently high, i.e., 4.02 dB, manifesting its large discrepancy between its predicted PL and the measured PL in indoor corridor channels.

Fig. 18 shows the measured PLs for three modes as well as the free-space PL, under $\theta_t = 45^\circ$, $\theta_r = 45^\circ$, and $d_1 = 6$ m. From this figure, the PLE of intelligent reflection mode shows an approximative value with the free-space PLE. In addition, a small gap of about 4 dB between the free-space PL and the measured PL is observed. In addition, the PL for intelligent reflection mode demonstrates a maximum gain of 10.6 dB than that for specular reflection mode and a maximum gain of 29.5 dB than that without RIS. Similarly to Fig. 11, as d_2 increases, the PL difference between the intelligent and specular reflection modes gets smaller. When d_2 is large enough, their coinciding PLs can be inferred.

Fig. 19 illustrates the PDP evolution vs d_1 and delay for three modes respectively, under $d_2 = 8$ m, $\theta_t = 45^\circ$, $\theta_r = 45^\circ$. Firstly, for the intelligent reflection mode, Fig. 19a exhibits a stationary spatial consistency on MPC evolution, despite it shows a small quantity of additional MPCs at 300 ns when d_1 is 5 ~ 13 m. For the specular reflection mode in Fig. 19b, there are plenty of additional MPCs covering all of the Tx positions. For the mode without RIS, a nonstationary spatial

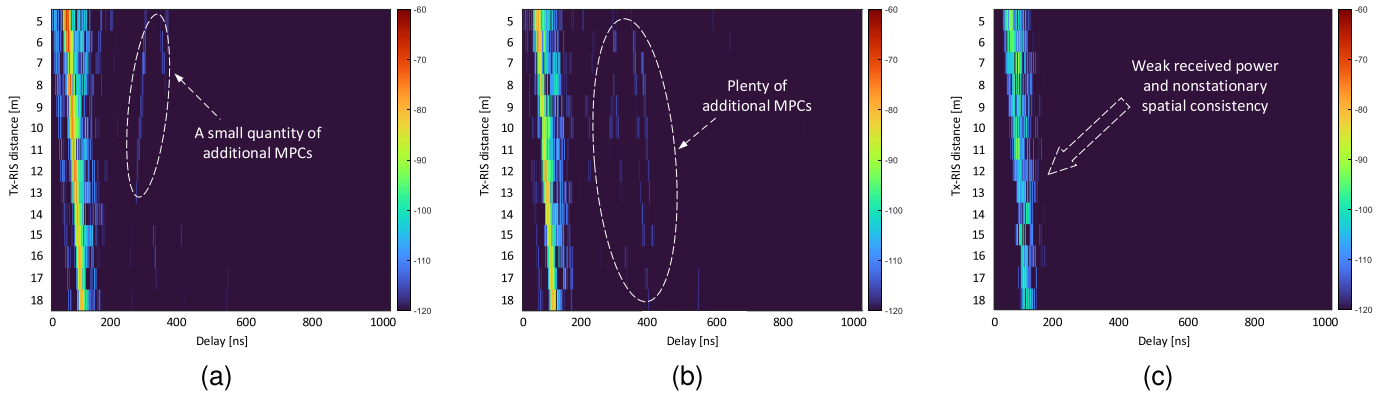


Fig. 19. PDP evolution vs delay and position. (a) Intelligent reflection. (b) Specular reflection. (c) Without RIS.

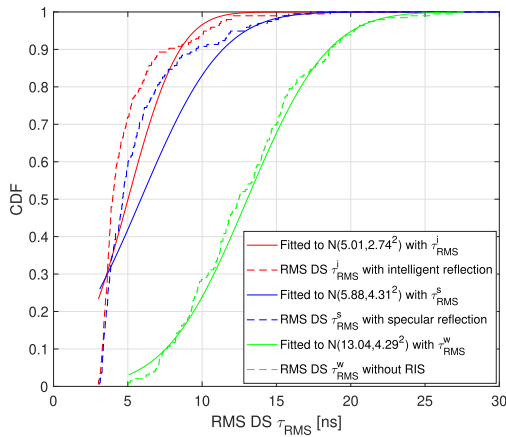


Fig. 20. Comparison of RMS DSs for three modes.

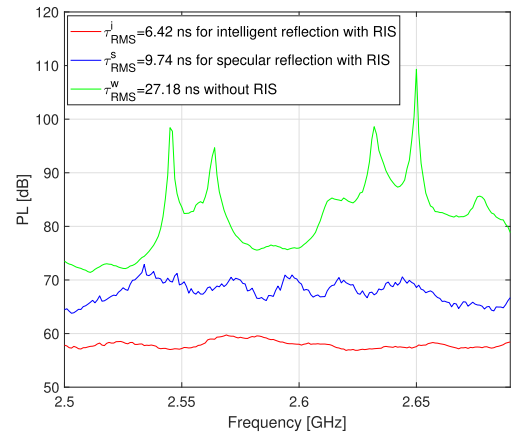


Fig. 21. Frequency stationarity for three modes.

evolution with weak power is observed in Fig. 19c. The above phenomena illustrate that intelligent reflection with RIS has a smoother spatial signal evolution when the transceiver moves.

Fig. 20 demonstrates the RMS DSs of three modes and the fitted Gaussian distributions $\mathcal{N}(\mu, \sigma^2)$, under $\theta_t = 45^\circ$ and $\theta_r = 45^\circ$. The means of these CDFs are 5.01 ns, 5.88 ns and 13.04 ns for the modes of intelligent reflection, specular reflection and without RIS respectively, as displayed in Table VII. This phenomenon illustrates that the channel time dispersion of intelligent reflection mode is lower than that of specular reflection mode even when Tx and Rx at the mirror positions *w.r.t.* RIS, because of the diffuse reflection of EM waves caused by the latter. The channel time dispersion without RIS is still the strongest, on account of its dominant scattering, diffraction, and diffuse reflection. In addition, it should be noted that these three means in indoor corridor scenario are respectively lower than those (8.42 ns, 10.79 ns and 37.55 ns respectively) in outdoor scenario, which indicates that the signal energy is better focused by RIS when in corridor channels.

Fig. 21 demonstrates the frequency stationarity within the measured bandwidth for three modes under $\theta_t = 45^\circ$, $\theta_r = 45^\circ$, $d_1 = 8$ m and $d_2 = 8$ m. Similarly to Fig. 16, the propagation signal without RIS shows the strongest frequency selective fading, followed by that of specular reflection with RIS. The intelligent reflection with RIS still has the flattest

TABLE IX
FITTING RESULTS FOR O2I MEASUREMENT

Parameters	α (PL_{FS}^{RIS})	β_2 (n_2)
Modified FI with measurement data	46.11	1.51
Modified FI with free-space data	47.64	1.8
Modified CI with measurement data	46.06	1.52
Modified CI with free-space data	46.06	2

fading environment. Their RMS DSs are respectively 27.18 ns, 9.74 ns and 6.42 ns, which accounts for the above phenomena theoretically according to the formulaic explanation of (17). This phenomenon evidences the superiority of intelligent beamforming by RIS against “plate metal” or “without RIS”, so as to support its claim of “customizing wireless channels”.

C. O2I Measurement

For the intelligent reflection mode in O2I measurement, the fitting results of the modified CI and FI models with the measured data as well as the free-space data are respectively summarized in Table IX. Note that only the measured data in left aisle is fitted to the models, where $\theta_t = 45^\circ$, $\theta_r = 45^\circ$, and $d_1 = 9$ m are fixed and the PLE on d_2 is taken into account in Table IX. The reference value $PL_{FS}^{RIS} = 46.06$ dB of the modified CI model is calculated under $\theta_t = 45^\circ$, $\theta_r = 45^\circ$, $d_1 = 9$ m, and $d_2 = 1$ m. From this table, we find that for both of the modified CI and FI models, the PLEs on d_2 with free-space data are significantly higher than those with

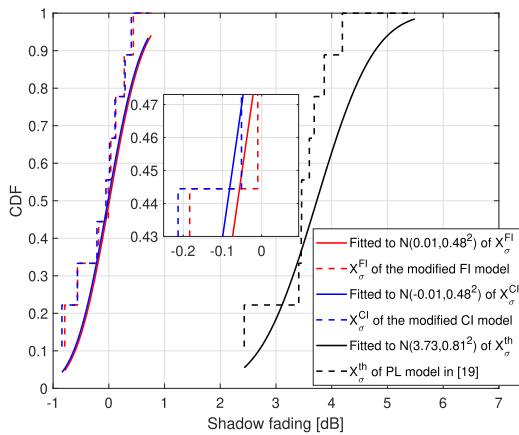


Fig. 22. SFs and the fitted CDFs in left aisle.

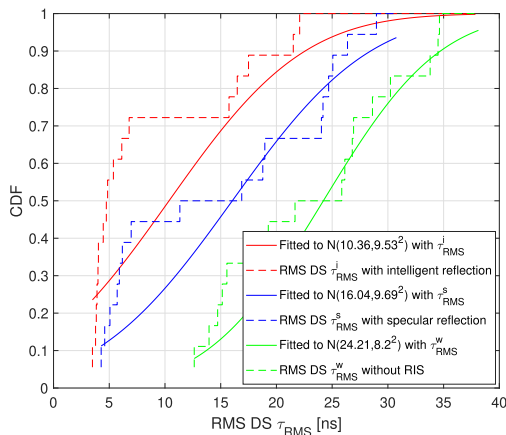


Fig. 23. Comparison of RMS DSs for three modes.

measurement data. This results from that in O2I measurement, there exists plentiful reflection and scattering caused by the surroundings such as desks and chairs.

Similar to Fig. 10 and Fig. 17, Fig. 22 exhibits the CDFs of SFs for the modified FI and CI models as well as the PL model in [19], where X_{σ}^{FI} , X_{σ}^{CI} and X_{σ}^{th} denote the same meanings as in outdoor and indoor measurements. As can be observed from Fig. 22, the modified FI and CI models have low mean values of 0.01 dB and -0.01 dB respectively, with the same standard deviation of 0.48 dB, which illustrate their high and similar prediction accuracy on PL in O2I scenarios. By contrast, the mean value for PL model in [19] is still high, i.e., 3.73 dB, indicating its large discrepancy between its predicted PL and the measured PL for O2I channels.

Fig. 23 shows the RMS DSs of three modes and the fitted Gaussian distributions $\mathcal{N}(\mu, \sigma^2)$. Their means are 10.36 ns, 16.04 ns and 24.21 ns respectively for the intelligent reflection, specular reflection and without RIS, as shown in Table VII. The channel time dispersion of intelligent reflection is still the lowest due to its property of focusing energy. Note that these two means for intelligent and specular reflection modes in classroom scenario are higher than those (8.42 ns and 10.79 ns) in outdoor scenario and those (5.01 ns and 5.88 ns) in corridor scenario. This indicates that the time dispersion for RIS-assisted channel in O2I scenario is strongest.

Fig. 24 shows the measured PLs for three modes in left and right aisles respectively, as well as the free-space PLs. Note that in right aisle, the Positions 1 and 2 are discarded because their propagation links with RIS are blocked by the teacher's table during the measurement. In left aisle shown in Fig. 24a, the PLE on d_2 of intelligent reflection mode is slightly lower than that of free-space PLE, resulting from the abundant scatters in this classroom. In addition, the PL for intelligent reflection mode demonstrates an improvement of about 7 dB than that for specular reflection mode and an improvement of about 25 ~ 30 dB than that without RIS. From Fig. 24b, the PLE on d_2 of intelligent reflection mode is greatly lower than that of free-space PLE in right aisle. Meanwhile, the PL for intelligent reflection mode demonstrates an improvement of about 15 ~ 20 dB than that for specular reflection mode and an improvement of about 20 ~ 25 dB than that without RIS. This indicates the coverage holes of specular reflection mode when Tx and Rx at the non-mirror positions *w.r.t.* RIS.

Fig. 25 demonstrates the frequency stationarity within the measured bandwidth for three modes at Position 5 in left and right aisles, respectively. From Fig. 25a, in left aisle, the RMS DSs are $\tau_{RMS}^i = 3.99$ ns, $\tau_{RMS}^s = 16.89$ ns and $\tau_{RMS}^w = 19.27$ ns respectively for the modes of intelligent reflection, specular reflection as well as without RIS. Their signals are respectively flat, slight frequency selective fading, and strong frequency selective fading, which can be theoretically explained by (17). As shown in Fig. 25b, in right aisle, the frequency stationarity for the modes of intelligent reflection and without RIS are similar to those in Fig. 25a. Nevertheless, the specular reflection mode in this figure illustrates a stronger frequency selective fading than that in left aisle. This attributes to that the specular reflection mode is incapable of covering the Rx positions in right aisle directly, where only the reflected and scattered signals arrive at Rx.

D. Summary of Measurement and Modeling

1) Channel measurement

On **PL**: In indoor and outdoor measurements, the measured PLE on distance or angle for *intelligent reflection with RIS* is approximate to the free-space PLE. In O2I measurement, the PLE with the measured data is prominently lower than that in free space, which may result from the abundant scattering in classroom. In addition, a difference value between the measured PL and the free-space PL is observed, indicating that the practical PL for RIS channel desires a more comprehensive characterization by new empirical model. In all of the three measurements, the *intelligent reflection with RIS* shows a significant improvement on PL covering multiple desired directions, against that of *specular reflection with RIS* as well as the mode *without RIS*.

On **RMS DS**: For *intelligent reflection with RIS*, *specular reflection with RIS*, and the mode *without RIS*, their means of RMS DSs are respectively 10.36 ns, 16.04 ns and 24.21 ns in O2I scenario, 8.42 ns, 10.79 ns and 37.55 ns in outdoor scenario, as well as 5.01 ns, 5.88 ns and 13.04 ns in indoor scenario. This indicates that for RIS-assisted channel, the time dispersion is the strongest in O2I scenario, followed by

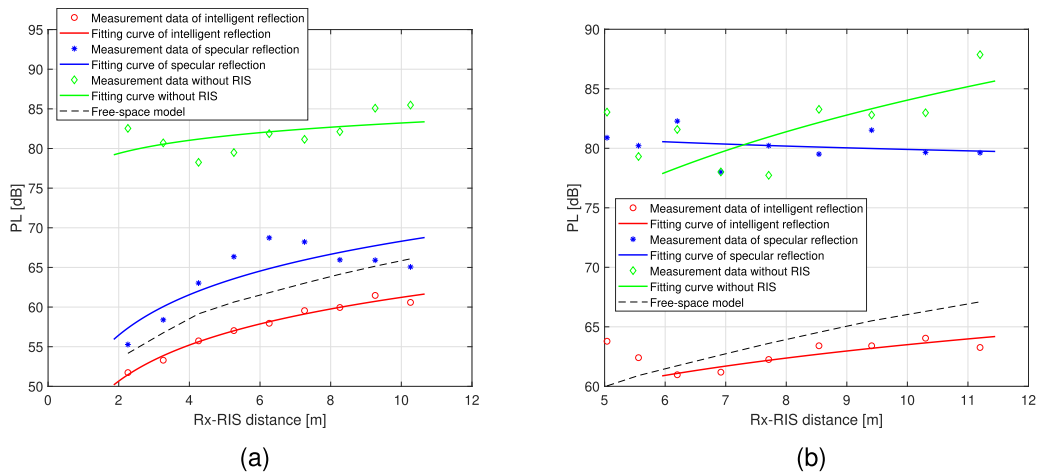


Fig. 24. PL comparison of measurement data and free-space data. (a) In left aisle. (b) In right aisle.

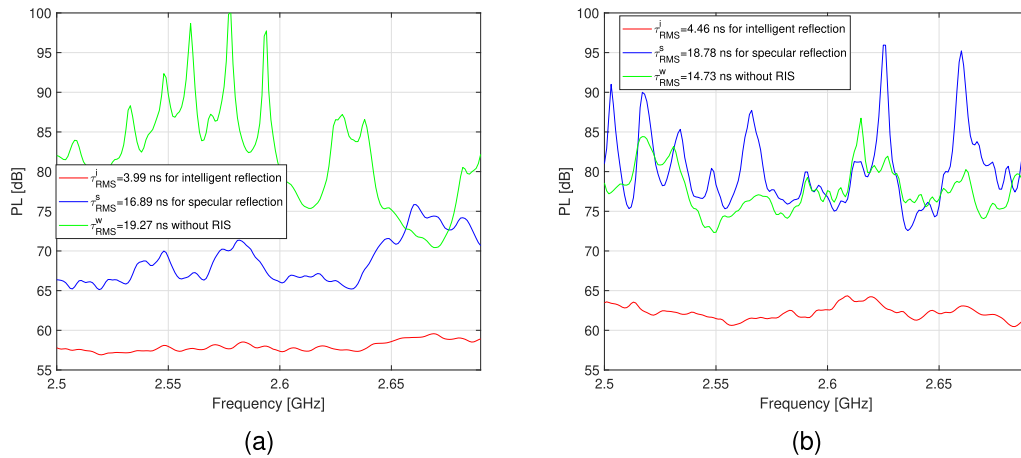


Fig. 25. Frequency stationarity for three modes. (a) In left aisle. (b) In right aisle.

outdoor scenario, and the weakest time dispersion occurs in indoor channel. Moreover, the *intelligent reflection with RIS* is evidenced to be favorable for focusing signal energy and reducing time dispersion.

On frequency stationarity: In all of the three measurements, the *intelligent reflection with RIS* demonstrates a flat propagation signal. By contrast, the *specular reflection with RIS* shows a slight but non-negligible frequency selective fading and the propagation mode *without RIS* manifests the strongest frequency selective fading. These phenomena evidence that the *intelligent reflection with RIS* is advantageous for enhancing frequency stationarity and may pave the way for promoting RIS-empowered high data rate transmission.

On spatial consistency: The MPC evolution for *intelligent reflection with RIS* shows a stationary spatial consistency as transceivers move. In addition, plenty of additional MPCs are observed for *specular reflection with RIS*. For the mode *without RIS*, a nonstationary spatial consistency with weak power is detected. These phenomena may have implications on the future research such as RIS-empowered beam tracking.

2) Channel modeling

On modeling accuracy: Both of the modified FI and CI models can be viewed as accurate and generalizable models to predict the PL characteristics of RIS-assisted channel covering distance and angle domains. For the discrepancy between their

predicted PLs and the measured PL, the mean values are nearly 0 dB in all of three scenarios and the standard deviations are respectively 2.53 dB, 2.46 dB and 0.48 dB in outdoor, indoor, and O2I scenarios. By contrast, the mean values of prediction discrepancy are respectively 2.68 dB, 4.02 dB and 3.73 dB by the free-space model. These phenomena confirm that for RIS-assisted channel, the proposed two models show a similar and high prediction accuracy. These results may have instructive meanings for future RIS-related PL modeling standardization.

On modeling complexity: The proposed two empirical models are inherited from the traditional FI and CI models respectively, which have been widely considered in reports, specifications and studies. The modified FI and CI models only parameterize several variables with the formal expression unchanged, while more comprehensively predicting the propagation characteristics for RIS-assisted channel. Thus, the modeling complexity can be reasonably acceptable and widely applicable for RIS-related practical deployment in the future.

VI. CONCLUSION

In this paper, we conducted multi-scenario broadband channel measurement campaigns and channel modeling for RIS-assisted SISO channel at 2.6 GHz. Utilizing the VNA-based measurement system and a fabricated RIS, three measurements

including outdoor, indoor and O2I scenarios were carried out, with 2096 channel acquisitions collected. In each scenario, three propagation modes including *intelligent reflection with RIS*, *specular reflection with RIS*, and the mode *without RIS* were measured. In addition, two modified empirical models including FI and CI, were proposed to cater for the cascaded characteristics of RIS-assisted channel. From the measurement results, the PL for *intelligent reflection with RIS* is significantly lower than that for *specular reflection with RIS* and that *without RIS*, which manifests its potential of improving the channel quality. The PLEs in outdoor and indoor scenarios show similar values as those in free space. Nevertheless, the PLE in O2I scenario is prominently lower than the free space value, which may be due to the plentiful scattering and reflections. Meanwhile, the proposed models are evidenced to be more accurate to characterize the practical PL compared to free-space model. Furthermore, for RIS-assisted channel, RMS DSs are highest in O2I scenario, followed by outdoor scenario, and lowest in indoor scenario. Among three propagation modes, the *intelligent reflection with RIS* is most favorable for focusing signal energy and reducing time dispersion. Additionally, the measurement results also illustrate that the *intelligent reflection with RIS* is beneficial to enhancing frequency stationarity. The MPC evolution for *intelligent reflection with RIS* shows a more stationary spatial consistency. In our future studies, more diverse and typical RIS-assisted communication scenarios such as urban macro cell (UMA) and MIMO, will be further measured and verified.

REFERENCES

- [1] M. W. Akhtar, S. A. Hassan, R. Ghaffar, H. Jung, S. Garg, and M. S. Hossain, "The shift to 6G communications: Vision and requirements," *Hum.-Centric Comput. Inf. Sci.*, vol. 10, no. 1, p. 53, Dec. 2020.
- [2] F. Tariq, M. R. A. Khandaker, K.-K. Wong, M. A. Imran, M. Bennis, and M. Debbah, "A speculative study on 6G," *IEEE Wireless Commun.*, vol. 27, no. 4, pp. 118–125, Aug. 2020.
- [3] M. Giordani, M. Polese, M. Mezzavilla, S. Rangan, and M. Zorzi, "Toward 6G networks: Use cases and technologies," *IEEE Commun. Mag.*, vol. 58, no. 3, pp. 55–61, Mar. 2020.
- [4] C.-X. Wang, J. Huang, H. Wang, X. Gao, X. You, and Y. Hao, "6G wireless channel measurements and models: Trends and challenges," *IEEE Veh. Technol. Mag.*, vol. 15, no. 4, pp. 22–32, Dec. 2020.
- [5] H. Tataria, M. Shafi, M. Dohler, and S. Sun, "Six critical challenges for 6G wireless systems: A summary and some solutions," *IEEE Veh. Technol. Mag.*, vol. 17, no. 1, pp. 16–26, Mar. 2022.
- [6] S. Basharat, S. A. Hassan, H. Pervaiz, A. Mahmood, Z. Ding, and M. Gidlund, "Reconfigurable intelligent surfaces: Potentials, applications, and challenges for 6G wireless networks," *IEEE Wireless Commun.*, vol. 28, no. 6, pp. 184–191, Dec. 2021.
- [7] E. C. Strinati et al., "Reconfigurable, intelligent, and sustainable wireless environments for 6G smart connectivity," *IEEE Commun. Mag.*, vol. 59, no. 10, pp. 99–105, Oct. 2021.
- [8] K. Feng, X. Li, Y. Han, and Y. Chen, "Joint beamforming optimization for reconfigurable intelligent surface-enabled MISO-OFDM systems," *China Commun.*, vol. 18, no. 3, pp. 63–79, Mar. 2021.
- [9] T. J. Cui, M. Q. Qi, X. Wan, J. Zhao, and Q. Cheng, "Coding metamaterials, digital metamaterials and programmable metamaterials," *Light, Sci. Appl.*, vol. 3, no. 10, pp. 1–9, Oct. 2014.
- [10] M. Di Renzo et al., "Smart radio environments empowered by reconfigurable intelligent surfaces: How it works, state of research, and the road ahead," *IEEE J. Sel. Areas Commun.*, vol. 38, no. 11, pp. 2450–2525, Nov. 2020.
- [11] Q. Wu and R. Zhang, "Towards smart and reconfigurable environment: Intelligent reflecting surface aided wireless network," *IEEE Commun. Mag.*, vol. 58, no. 1, pp. 106–112, Jan. 2020.
- [12] Y. Lin, S. Jin, M. Matthaiou, and X. You, "Channel estimation and user localization for IRS-assisted MIMO-OFDM systems," *IEEE Trans. Wireless Commun.*, vol. 21, no. 4, pp. 2320–2335, Apr. 2022.
- [13] K. Feng, X. Li, Y. Han, S. Jin, and Y. Chen, "Physical layer security enhancement exploiting intelligent reflecting surface," *IEEE Commun. Lett.*, vol. 25, no. 3, pp. 734–738, Mar. 2021.
- [14] K. Feng, Q. Wang, X. Li, and C.-K. Wen, "Deep reinforcement learning based intelligent reflecting surface optimization for MISO communication systems," *IEEE Wireless Commun. Lett.*, vol. 9, no. 5, pp. 745–749, May 2020.
- [15] L. Jiang, X. Li, M. Matthaiou, and S. Jin, "Joint user scheduling and phase shift design for RIS assisted multi-cell MISO systems," *IEEE Wireless Commun. Lett.*, vol. 12, no. 3, pp. 431–435, Mar. 2023.
- [16] J. Sang et al., "Coverage enhancement by deploying RIS in 5G commercial mobile networks: Field trials," *IEEE Wireless Commun.*, early access, Dec. 26, 2022, doi: [10.1109/MWC.011.2200356](https://doi.org/10.1109/MWC.011.2200356).
- [17] J. Huang et al., "Reconfigurable intelligent surfaces: Channel characterization and modeling," *Proc. IEEE*, vol. 110, no. 9, pp. 1290–1311, Sep. 2022.
- [18] W. Tang et al., "Wireless communications with reconfigurable intelligent surface: Path loss modeling and experimental measurement," *IEEE Trans. Wireless Commun.*, vol. 20, no. 1, pp. 421–439, Jan. 2021.
- [19] W. Tang et al., "Path loss modeling and measurements for reconfigurable intelligent surfaces in the millimeter-wave frequency band," *IEEE Trans. Commun.*, vol. 70, no. 9, pp. 6259–6276, Sep. 2022.
- [20] R. Zhou et al., "Modeling and measurements for multi-path mitigation with reconfigurable intelligent surfaces," in *Proc. 16th Eur. Conf. Antennas Propag. (EuCAP)*, Madrid, Spain, Mar. 2022, pp. 1–5.
- [21] S. W. Ellingson, "Path loss in reconfigurable intelligent surface-enabled channels," in *Proc. IEEE 32nd Annu. Int. Symp. Pers., Indoor Mobile Radio Commun. (PIMRC)*, Helsinki, Finland, Sep. 2021, pp. 829–835.
- [22] J. C. B. Garcia, A. Sibille, and M. Kamoun, "Reconfigurable intelligent surfaces: Bridging the gap between scattering and reflection," *IEEE J. Sel. Areas Commun.*, vol. 38, no. 11, pp. 2538–2547, Nov. 2020.
- [23] F. H. Danufane, M. D. Renzo, J. de Rosny, and S. Tretjakov, "On the path-loss of reconfigurable intelligent surfaces: An approach based on Green's theorem applied to vector fields," *IEEE Trans. Commun.*, vol. 69, no. 8, pp. 5573–5592, Aug. 2021.
- [24] Ö. Özdogan, E. Björnson, and E. G. Larsson, "Intelligent reflecting surfaces: Physics, propagation, and pathloss modeling," *IEEE Wireless Commun. Lett.*, vol. 9, no. 5, pp. 581–585, May 2020.
- [25] M. Najafi, V. Jamali, R. Schober, and H. V. Poor, "Physics-based modeling and scalable optimization of large intelligent reflecting surfaces," *IEEE Trans. Commun.*, vol. 69, no. 4, pp. 2673–2691, Apr. 2021.
- [26] E. Basar and I. Yildirim, "Reconfigurable intelligent surfaces for future wireless networks: A channel modeling perspective," *IEEE Wireless Commun.*, vol. 28, no. 3, pp. 108–114, Jun. 2021.
- [27] G. Sun et al., "A 3D wideband channel model for RIS-assisted MIMO communications," *IEEE Trans. Veh. Technol.*, vol. 71, no. 8, pp. 8016–8029, Aug. 2022.
- [28] G. Sun, R. He, Z. Ma, B. Ai, and Z. Zhong, "A 3D geometry-based non-stationary MIMO channel model for RIS-assisted communications," in *Proc. IEEE 94th Veh. Technol. Conf. (VTC-Fall)*, Sep. 2021, pp. 1–5.
- [29] Y. Sun, C.-X. Wang, J. Huang, and J. Wang, "A 3D non-stationary channel model for 6G wireless systems employing intelligent reflecting surfaces with practical phase shifts," *IEEE Trans. Cognit. Commun. Netw.*, vol. 7, no. 2, pp. 496–510, Jun. 2021.
- [30] H. Jiang et al., "A general wideband non-stationary stochastic channel model for intelligent reflecting surface-assisted MIMO communications," *IEEE Trans. Wireless Commun.*, vol. 20, no. 8, pp. 5314–5328, Aug. 2021.
- [31] W. Tang et al., "On channel reciprocity in reconfigurable intelligent surface assisted wireless networks," *IEEE Wireless Commun.*, vol. 28, no. 6, pp. 94–101, Dec. 2021.
- [32] X. Pei et al., "RIS-aided wireless communications: Prototyping, adaptive beamforming, and indoor/outdoor field trials," *IEEE Trans. Commun.*, vol. 69, no. 12, pp. 8627–8640, Dec. 2021.
- [33] G. C. Trichopoulos et al., "Design and evaluation of reconfigurable intelligent surfaces in real-world environment," *IEEE Open J. Commun. Soc.*, vol. 3, pp. 462–474, 2022.
- [34] X. Tan, Z. Sun, J. M. Jornet, and D. Pados, "Increasing indoor spectrum sharing capacity using smart reflect-array," in *Proc. IEEE Int. Conf. Commun. (ICC)*, Kuala Lumpur, Malaysia, May 2016, pp. 1–6.

- [35] A. Araghi et al., "Reconfigurable intelligent surface (RIS) in the sub-6 GHz band: Design, implementation, and real-world demonstration," *IEEE Access*, vol. 10, pp. 2646–2655, 2022.
- [36] J. Rains et al., "High-resolution programmable scattering for wireless coverage enhancement: An indoor field trial campaign," *IEEE Trans. Antennas Propag.*, vol. 71, no. 1, pp. 518–530, Jan. 2023.
- [37] J.-B. Gros, V. Popov, M. A. Odit, V. Lenets, and G. Lerosey, "A reconfigurable intelligent surface at mmWave based on a binary phase tunable metasurface," *IEEE Open J. Commun. Soc.*, vol. 2, pp. 1055–1064, 2021.
- [38] A. Mudonhi, M. Lotti, A. Clemente, R. D'Errico, and C. Oestges, "RIS-enabled mmWave channel sounding based on electronically reconfigurable transmitarrays," in *Proc. 15th Eur. Conf. Antennas Propag. (EuCAP)*, Dusseldorf, Germany, Mar. 2021, pp. 1–5.
- [39] S. Kayraklık, I. Yildirim, Y. Gevez, E. Basar, and A. Görçin, "Indoor coverage enhancement for RIS-assisted communication systems: Practical measurements and efficient grouping," in *Proc. IEEE Int. Conf. Commun. (ICC)*, Roma, Roma, Italy, Jun. 2023, pp. 485–490.
- [40] S. Keşir, S. Kayraklık, İ. Hökelek, A. E. Pusane, E. Basar, and A. Görçin, "Measurement-based characterization of physical layer security for RIS-assisted wireless systems," in *Proc. IEEE 97th Veh. Technol. Conf. (VTC-Spring)*, Florence, Italy, Jun. 2023, pp. 1–6.
- [41] M. C. Wicks, E. L. Mokole, S. D. Blunt, R. S. Schneible, and V. J. Amuso, *Principles of Waveform Diversity and Design*. NC, USA: SciTech, 2011.
- [42] *Base Station (BS) Radio Transmission and Reception*, document TS 38.104 (V16.13.0), 3GPP, Sep. 2022.
- [43] B. Gao et al., "Propagation characteristics of RIS-assisted wireless channels in corridors: Measurements and analysis," in *Proc. IEEE/CIC Int. Conf. Commun. China (ICCC)*, Foshan, China, Aug. 2022, pp. 550–554.
- [44] J. Sang et al., "Quantized phase alignment by discrete phase shifts for reconfigurable intelligent surface-assisted communication systems," 2023, *arXiv:2303.13046*.
- [45] P. Zhang, B. Yang, C. Yi, H. Wang, and X. You, "Measurement-based 5G millimeter-wave propagation characterization in vegetated suburban macrocell environments," *IEEE Trans. Antennas Propag.*, vol. 68, no. 7, pp. 5556–5567, Jul. 2020.
- [46] *Study on Channel Model for Frequency From 0.5 to 100 GHz*, document TR 38.901 (V16.1.0), 3GPP, Dec. 2019.
- [47] *Multipath Propagation and Parameterization of Its Characteristics*, ITU-R, ITU-R TR P. 1407-6, 2017.



Jian Sang (Graduate Student Member, IEEE) received the B.S. degree from Northeastern University, China, in 2018, and the joint M.S. degree from the Shanghai Advanced Research Institute, Chinese Academy of Sciences, and Shanghai University, in 2021. He is currently pursuing the Ph.D. degree in communication and information system with the National Mobile Communications Research Laboratory, Southeast University. His research interests include channel measurement, channel modeling, and precoding design in reconfigurable intelligent surface (RIS)-assisted wireless communications.



Mingyong Zhou received the B.S. degree in communication engineering from the School of Communication and Information Engineering, Nanjing University of Posts and Telecommunications, China, in 2020, and the M.S. degree in information and communication engineering from the School of Information Science and Engineering, Southeast University, China, in 2023, where he is currently pursuing the Ph.D. degree with the National Mobile Communications Research Laboratory. His research interests include channel measurement, channel modeling, and metasurface-based wireless communication system design and implementation.



Jifeng Lan (Graduate Student Member, IEEE) received the B.S. degree from Xidian University, China, in 2021. He is currently pursuing the M.S. degree in communication and information system with the National Mobile Communications Research Laboratory, Southeast University. His research interests include channel measurement and channel modeling.



Boning Gao received the B.S. degree in information and communication engineering from the School of Information Science and Engineering, Southeast University, China, in 2022, where he is currently pursuing the M.S. degree in communication and information system with the National Mobile Communications Research Laboratory. His research interests include RIS-related wireless communications and channel models.



Wankai Tang (Member, IEEE) received the B.S., M.S., and Ph.D. degrees from Southeast University, Nanjing, China, in 2011, 2014, and 2021, respectively. He was with National Instruments, Shanghai, China, from 2014 to 2016. He is currently with the Faculty of the National Mobile Communications Research Laboratory, Southeast University. His research interests include modeling and prototyping of reconfigurable intelligent surface (RIS)-empowered wireless communication systems. He received the IEEE Jack Neubauer Memorial Award, the IEEE COMSOC Asia-Pacific Outstanding Paper Award in 2023, the *China Communications Best Paper Award* in 2021, and the *Electronics Letters Best Paper Award* in 2020.



Xiao Li (Member, IEEE) received the Ph.D. degree in communication and information systems from Southeast University, Nanjing, China, in 2010.

Then, she joined the School of Information Science and Engineering, Southeast University, where she has been a Professor of information systems and communications, since July 2020. From January 2013 to January 2014, she was a Post-Doctoral Fellow with The University of Texas at Austin, Austin, TX, USA. Her current research interests include massive MIMO, reconfigurable intelligent surface assisted communications, and intelligent communications.

Dr. Li was a recipient of the 2013 National Excellent Doctoral Dissertation of China for her Ph.D. dissertation. She serves as an Associate Editor for *IEEE TRANSACTIONS ON WIRELESS COMMUNICATIONS*, *IEEE WIRELESS COMMUNICATIONS LETTERS*, and the *Electronics Letters*; and a Guest Editor for the *Digital Communications and Networks*.



Shi Jin (Senior Member, IEEE) received the B.S. degree in communications engineering from the Guilin University of Electronic Technology, Guilin, China, in 1996, the M.S. degree from the Nanjing University of Posts and Telecommunications, Nanjing, China, in 2003, and the Ph.D. degree in information and communications engineering from Southeast University, Nanjing, in 2007. From June 2007 to October 2009, he was a Research Fellow with the Adastral Park Research Campus, University College London, London, U.K. He is currently with

the Faculty of the National Mobile Communications Research Laboratory, Southeast University. His research interests include wireless communications, random matrix theory, and information theory. He and his coauthors received the 2011 IEEE Communications Society Stephen O. Rice Prize Paper Award in the field of communication theory, the 2022 Best Paper Award, the 2010 Young Author Best Paper Award by the IEEE Signal Processing Society, and the 2023 IEEE Jack Neubauer Memorial Award by the IEEE Vehicular Technology Society. He is serving as an Area Editor for *IEEE TRANSACTIONS ON COMMUNICATIONS* and *IET Electronics Letters*. He was an Associate Editor of *IEEE TRANSACTIONS ON WIRELESS COMMUNICATIONS*, *IEEE COMMUNICATIONS LETTERS*, and *IET Communications*.



Ertugrul Basar (Fellow, IEEE) received the Ph.D. degree from Istanbul Technical University in 2013. He is currently an Associate Professor with the Department of Electrical and Electronics Engineering, Koç University, Istanbul, Turkey, and the Director of the Communications Research and Innovation Laboratory (CoreLab). He is the author/coauthor of around 150 international journal publications and ten patents that received more than 12,000 citations. His primary research interests include beyond 5G and 6G wireless networks, communication theory and systems, reconfigurable intelligent surfaces, index modulation, waveform design, and signal processing for communications. He was a Young Member of the Turkish Academy of Sciences in 2017. In the past, he served as an Editor/a Senior Editor for many journals, including IEEE COMMUNICATIONS LETTERS (2016–2022), IEEE TRANSACTIONS ON COMMUNICATIONS (2018–2022), *Physical Communication* (2017–2020), and IEEE ACCESS (2016–2018). He is an Editor of *Frontiers in Communications and Networks*.



Cen Li received the master's degree from the Nanjing University of Posts and Telecommunications. As an industry professor in Jiangsu Province, he currently holds a positions of the Deputy General Manager of China Information Consulting Designing Institute Company Ltd., the Executive Director of the China International Engineering Consulting Association, the Director of the China Communications Enterprise Association, and the Deputy Secretary-General of the Nanjing Youth Federation. He has engaged in technical and management work

related to communication engineering projects. The project he led, "South-to-North Water Transfer Eastern Route Communication Dispatching Project," was awarded the WSIS Winner Award by the International Telecommunication Union. He has presided over three provincial and municipal scientific research projects, such as industrial upgrading and transformation of the province and city, and has won two provincial communications industry science and technology progress awards. He has applied for 15 invention patents in the field of communications and six has been authorized.



Qiang Cheng (Senior Member, IEEE) received the B.S. and M.S. degrees from the Nanjing University of Aeronautics and Astronautics, Nanjing, Jiangsu, China, in 2001 and 2004, respectively, and the Ph.D. degree from Southeast University, Nanjing, in 2008.

In 2008, he joined the State Key Laboratory of Millimeter Waves, Southeast University, where he was involved in the development of metamaterials and meta-devices. He is currently a Full Professor with the Radio Department, Southeast University. He leads a group of Ph.D. students and master's

students in the area of metamaterials, tunable microwaves circuits, microwave imaging, and terahertz systems. He has authored or coauthored more than 100 publications, with citation over 2000 times.

Dr. Cheng was a recipient of the 2010 Best Paper Award from the *New Journal of Physics*, the Chinas Top Ten Scientific Advances of 2010, and the Second Class National Natural Science Award in 2014. He served as the Vice Chair for the 2008 and 2010 International Workshop on Metamaterials, Nanjing.



Tie Jun Cui (Fellow, IEEE) received the B.Sc., M.Sc., and Ph.D. degrees in electrical engineering from Xidian University, Xi'an, China, in 1987, 1990, and 1993, respectively.

In March 1993, he joined the Department of Electromagnetic Engineering, Xidian University, and was promoted to an Associate Professor in November 1993. From 1995 to 1997, he was a Research Fellow with Institut für Hochfrequenztechnik und Elektronik (IHE), University of Karlsruhe, Germany.

In July 1997, he joined the Center for Computational

Electromagnetics, Department of Electrical and Computer Engineering, University of Illinois at Urbana–Champaign, first as a Post-Doctoral Research Associate and then a Research Scientist. In September 2001, he was a Cheung-Kong Professor with the Department of Radio Engineering, Southeast University, Nanjing, China, where he is currently the Chief Professor and the Director of the State Key Laboratory of Millimeter Waves. He is also the Founding Director of the Institute of Electromagnetic Space, Southeast University. He proposed the concepts of digital coding and programmable metamaterials and realized their first prototypes, based on which he founded the new direction of information metamaterials, bridging the physical world and digital world. He is the first author of books *Metamaterials Theory, Design, and Applications* (Springer, November 2009); *Metamaterials: Beyond Crystals, Noncrystals, and Quasicrystals* (CRC Press, March 2016); and *Information Metamaterials* (Cambridge University Press, 2021). He has published over 600 peer-reviewed journal articles, which have been cited by more than 61,000 times (H-Factor is 122), and licensed over 160 patents. His research interests include metamaterials and computational electromagnetics.

Dr. Cui is an Academician of the Chinese Academy of Science. He received the Research Fellowship from the Alexander von Humboldt Foundation, Bonn, Germany, in 1995; the Young Scientist Award from the International Union of Radio Science in 1999; the Cheung Kong Professor by the Ministry of Education, China, in 2001; and the National Science Foundation of China for Distinguished Young Scholars in 2002. He also received the Natural Science Award (first class) from the Ministry of Education, China, in 2011; the National Natural Science Awards of China (twice) in 2014 and 2018; the Clarivate Highly Cited Researchers Awards, from 2019 to 2023; the Outstanding Contribution Award for *Light: Science and Applications*; and the Frontiers of Science Award in the First International Congress of Basic Science, in 2023. He also received many best paper awards in prestigious journals and conferences. His research works have selected as one of the most exciting peer-reviewed optics research "Optics in 2016" by the Optical Society of America, ten Breakthroughs of China Science in 2010, ten Breakthroughs of Science and Technology in National Universities of China in 2021, and many Research Highlights in a series of journals. His work has been widely reported by Nature News, *MIT Technology Review*, *Scientific American*, *Discover*, and *New Scientists*. He served as an Associate Editor for IEEE TRANSACTIONS ON GEOSCIENCE AND REMOTE SENSING; and a Guest Editor for *Science China Information Sciences*, *Science Bulletin*, IEEE TRANSACTIONS ON MICROWAVE THEORY AND TECHNIQUES, IEEE JOURNAL OF EMERGING TECHNOLOGIES IN CIRCUITS AND SYSTEM, *Applied Physics Letters*, *Engineering*, and *Research*. Currently, he is the Chief Editor of *Metamaterial* short books (Cambridge University Press), an Editor of *Materials Today Electronics*, an Associate Editor of *Research*, and the Editorial Board Members of *National Science Review*, *eLight*, *Photonix*, *Advanced Optical Materials*, *Small Structure*, *Advanced Photonics Research*, and *Journal of Physics: Photonics*. He has presented more than 100 keynote and plenary talks in academic conferences, symposiums, and workshops.